

DTIC
8713-EN-01

AD

**EARTHQUAKE ENGINEERING SUPPORT
PHASE 3**

Final Technical Report

by

R S Steedman

November 1999

United States Army

EUROPEAN OFFICE OF THE U.S. ARMY

London England

CONTRACT NUMBER: N68171-99-C-9021

PRINCIPAL INVESTIGATOR: DR R S STEEDMAN

Approved for Public Release; distribution unlimited

DTIC QUALITY INSPECTED 1

20000118 090

SUMMARY

A large experimental study has been undertaken at the USAE Waterways Experiment Station (WES) as part of the ongoing U.S. Army Engineer Earthquake Engineering Research Program (EQEN) to investigate the behavior of liquefying soil materials. In this study, experiments have addressed the development of excess pore pressure and the onset of liquefaction within a deep soil column using the new large geotechnical centrifuge and earthquake shaker. The approach adopted was to use standard procedures for the assessment of liquefaction resistance to derive values of the strength reduction factor K_σ from the experimental results, with the object of confirming the validity of the simplified K_σ approach under high effective overburden stresses. Data of excess pore pressures from the experiments showed the soil column reaching a state of initial liquefaction over a range of depths up to around 20 m (65 ft) under moderate levels of base input shaking, and from this data values of K_σ could be derived. As expected, these showed considerable variability, being sensitive to initial assumptions. More significantly, at greater depths, the development of excess pore pressure was capped and despite continued shaking at similar amplitude, the development of excess pore pressure did not reach a sufficient level to cause initial liquefaction. Similar observations have been found in the literature from torsional shear tests. It is concluded that the effects of confining stress and the strain boundary conditions which exist in the soil column in the field are significant in controlling the development of excess pore pressure. In the absence of initial liquefaction, the use of the K_σ factor to assess the cyclic resistance of the soil is not considered appropriate.

LIST OF KEYWORDS

liquefaction
centrifuge
earthquake
model
experiment
sand

TABLE OF CONTENTS

| | |
|--|-----|
| Summary | i |
| List of Keywords | ii |
| Table of Contents | iii |
| 1 Introduction | 1 |
| 2 The Army centrifuge, earthquake shaker and specimen container | 2 |
| 2.1 The Army centrifuge and earthquake actuator | 2 |
| 2.2 Specimen container (the ESB box) | 5 |
| 2.3 Dynamic response of the soil container and specimen | 8 |
| 3 Model test configuration and instrumentation | 13 |
| 3.1 Outline of experiments | 13 |
| 3.2 Summary of model test series | 13 |
| 3.3 Materials | 16 |
| 3.4 Instrumentation layout | 17 |
| 4 Analysis and interpretation of earthquake model test data | 21 |
| 4.1 State-of-practice for liquefaction assessment | 21 |
| 4.2 Research problem | 22 |
| 4.3 Calculation of K_σ from measurements made in a soil column | 24 |
| 4.4 SHAKE analysis of soil column | 27 |
| 4.5 Comparison with published Magnitude Scaling Factors | 28 |
| 4.6 Comparison between centrifuge K_σ and laboratory K_σ results | 32 |
| 4.7 Comparison with 'Stress focus' concept | 35 |
| 4.8 Stress path analysis | 37 |
| 4.9 Data of excess pore pressures | 41 |
| 5 Conclusions | 45 |
| 6 References | 46 |

Appendix A Earthquake model test dataset

Appendix B Stress path analysis

1 INTRODUCTION

The current state of practice for determining the performance of soils that undergo earthquake induced shear strain and consequently pore water pressure build-up in saturated soils is to determine if a soil will or will not liquefy. The performance and safety of structures are based on rigid sliding block/slices limit equilibrium methods to determine slip-plane stability and deformation using residual strengths in the case of liquefaction.

In the standard design methods for the assessment of liquefaction resistance of saturated sands under high effective confining stresses, reliance has been placed on laboratory test data which show a general reduction in the cyclic strength of the soil. This is accounted for in the widely used 'simplified procedure' through the use of the K_σ factor, Seed and Harder (1990). At high effective confining stresses, the K_σ factor can require a substantial reduction in the liquefaction resistance of the soil. Studies in the literature indicate that values of K_σ calculated by different researchers can vary widely and that extrapolation of the simplified procedure to depths greater than 15m is not supported by case history data from the field.

A large experimental program has been undertaken at the USAE Waterways Experiment Station, Vicksburg Mississippi using the new centrifuge research facility and earthquake shaker.

2 THE ARMY CENTRIFUGE, EARTHQUAKE SHAKER AND SPECIMEN CONTAINER

2.1 *The Army Centrifuge and earthquake actuator*

The design specification of the centrifuge was finalised following a broad ranging review of the typical field structures and problems with which the Corps is principally engaged Ledbetter (1991). The design of the centrifuge was based on the French designed Acutronic 661, 665, and 680 series of geotechnical centrifuges. Similar in its physical dimensions to the 680 model, the WES centrifuge (Fig. 2.1) is distinguished by its significantly higher performance capability. Key characteristics are summarised in Table 2.1.

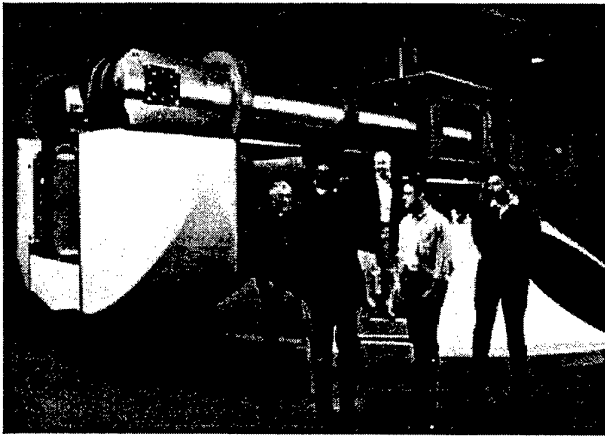


Figure 2.1 The Army Centrifuge


| | |
|--|---------------|
|  Army Centrifuge | |
| Radius to platform | 6.5 m |
| Payload at 143 g | 8000 kg |
| Payload at 350 g | 2000 kg |
| Capacity | 1144 g tonnes |

Table 2.1 Key performance characteristics

The earthquake actuator used in the present series of experiments was a large mechanical shaker designed to provide a single frequency input motion of variable duration to the base of the specimen container. The actuator was based on a design successfully developed at Cambridge University known as the SAM actuator, Madabushi et al. (1996), energy is stored in flywheels in the form of angular momentum. The advantages of this design are that it is a simple mechanical system capable of high g operation, with low cost of construction. Disadvantages include a restricted ability to control the amplitude of input motions and difficulties in controlling high frequency vibrations under low amplitude operations.

The use of a single frequency of input motion was considered appropriate to the nature of the experiments, the results of which would be compared with laboratory cyclical element tests and standard design methods for liquefaction assessment which were based on numbers of 'equivalent' uniform cycles.

The general arrangement of the actuator is shown in Figs 2.2 and 2.3. Fig 2.4 shows a photograph of the actuator with the motor on the right and high vertical support walls enclosing the shaking table and specimen container on the left.

A system of linkages and eccentrics transfer the stored energy of the fly wheels to the shaking platform and thence into the soil specimen, Figure 2.3. A hydraulic or electrical motor drives the flywheels up to full speed, and then, on a signal, a high speed clutch grabs the oscillating shaft and transfers energy into the model until another signal releases it again. Clearly the frequency of the oscillation is directly proportional to the speed of the motor (and flywheels). The amplitude is controlled by the arrangement of the eccentrics; three displacement amplitudes for the platform are available ($\pm 0.49\text{mm}$, $\pm 1.47\text{mm}$ and $\pm 4.41\text{mm}$).

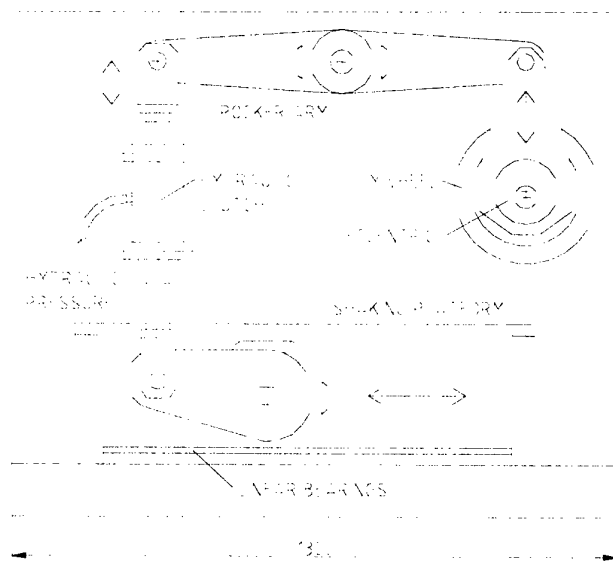


Figure 2.2 Elevation of the earthquake actuator, Butler (1999)

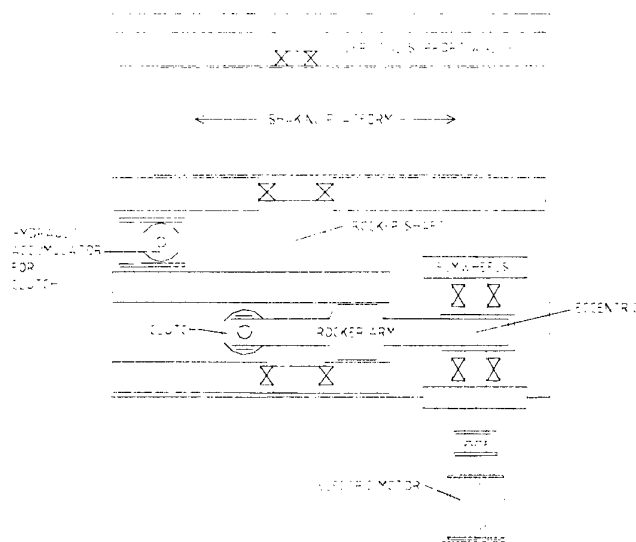


Figure 2.3 Plan of the earthquake actuator, Butler (1999)

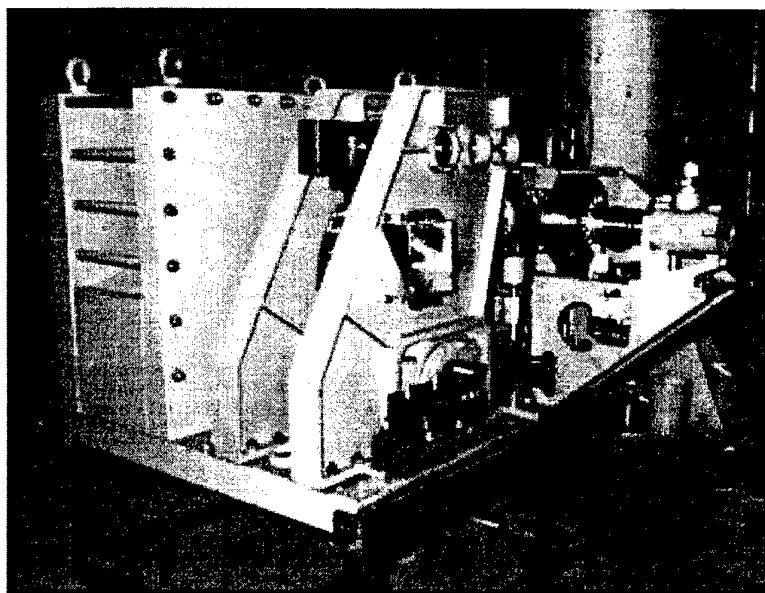


Figure 2.4 The earthquake actuator, seen from the rear

The shaker is designed (structurally) for operation up to 150g, at which the maximum load capacity of the base oscillating platform is reached (75 tonnes, or 500 kg at 1g). The design maximum lateral force which the mechanism may exert on the platform is 30 tonnes, and the maximum frequency at which the shaker may be safely operated is 150 Hz (eg. 1Hz prototype at 150g, or 3Hz prototype at 50g).

2.2 Specimen container (the ESB box)

The specimen is built within a hollow rectangular model container (ESB) comprising a series of aluminium alloy rings stacked one above the other, and separated by a elastic medium, Figure 2.5. Several of these chambers have been constructed, and extensive dynamic analysis and testing has been carried out to determine their dynamic response characteristics, Butler (1999).

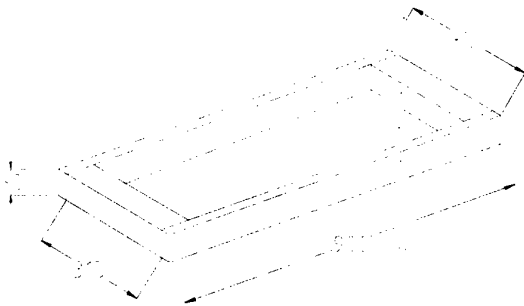
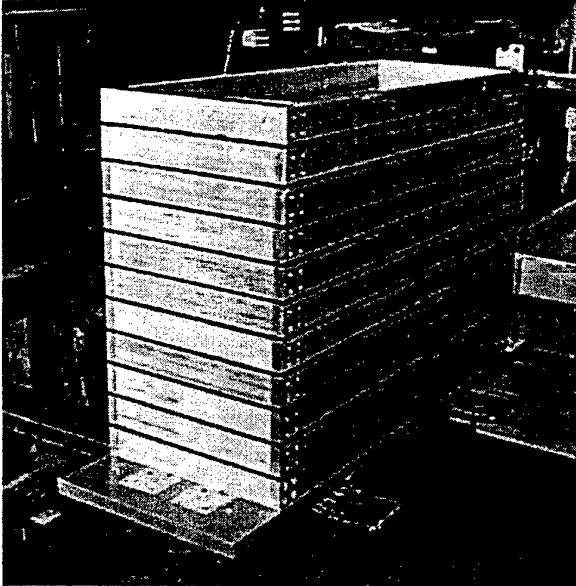
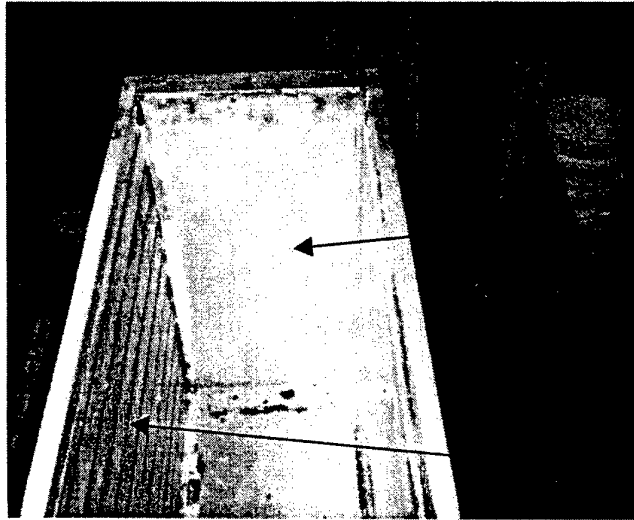


Figure 2.5 The WES ESB container, Mk II, and an individual aluminium ring

The model container has internal dimensions of 627mm deep by 315mm wide by 796mm long. Each of the eleven aluminium alloy rings is 50mm high. The rings are not stiff enough along their long dimension to support the outward pressure from the soil inside under high g , but they are supported by the massive vertical reaction walls of the shaker unit itself. A rubber sheet separates the rings from the steel walls on either side. This concept has the added advantage of raising the centre of gravity of the reaction mass in line with the centre of gravity of the specimen, thus minimising eccentric forces which may lead to rocking.

Up each of the end walls of the ESB are positioned thin metal sheets, termed shear sheets, fixed securely to the base of the chamber, which can accommodate the

complementary shear force generated by the horizontal shaking on vertical planes within the specimen and transmit that force to the base of the container, Fig. 2.6. This improves the uniformity of the stress field at each elevation along the model, reducing the tendency for the chamber to 'rock'.



shear sheet, with rough sand finish, bolted to the floor of the ESB and laid up against the end wall

stacked aluminium rings, separated by elastic sealant

SHEAR SHEET, ON END WALL
ESB #2

Figure 2.6 Shear sheets at each end of the ESB

In the bottom of the model chamber, slotted metal plates were used to create flow channels across the base to improve the uniformity of the saturation process. These slots were filled with a coarse sand, to create a level base for the specimen. To ensure accuracy of weighing the specimen, the ports and slots were filled with fluid prior to the dry pluviation of the specimen proper. The combination of slots and coarse sand was designed to ensure full shear transfer into the specimen, forming a 'rough' base, Fig. 2.7.

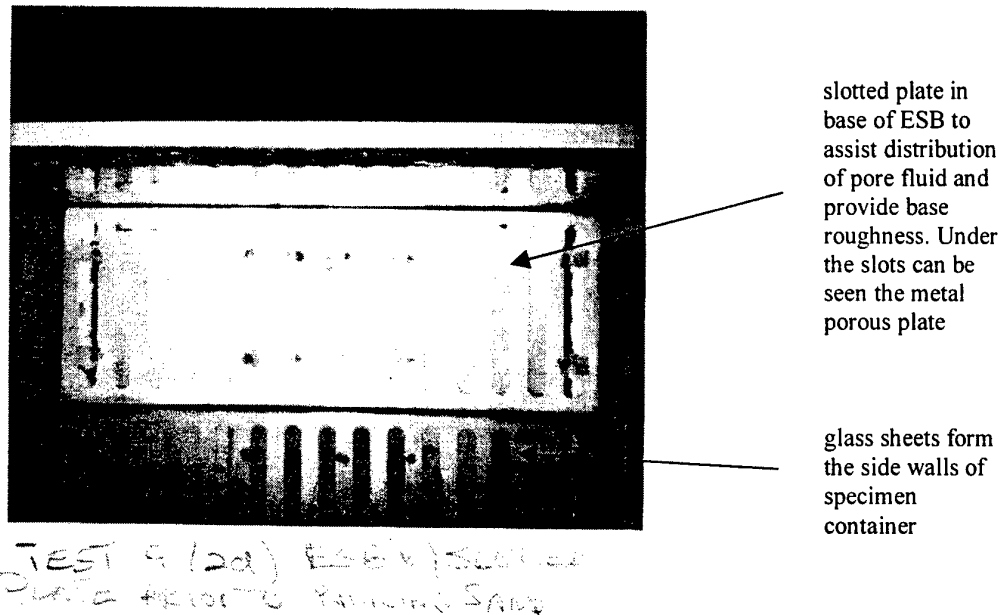


Figure 2.7 Slotted plate in the base of the ESB

The ESB concept is to create an equivalent shear beam with an average stiffness comparable to the stiffness of the soil specimen. Expressed rigorously, the concept is more accurately defined as achieving a dynamic response which does not significantly influence the behaviour of the soil specimen inside. For certain classes of experiment, it may be expected that the stiffness of the soil (at least near the end walls) would not reduce significantly during shaking due to excess pore pressure rise, and the stiffness of the chamber may be designed accordingly, perhaps considering a shear modulus appropriate to the level of dynamic strain expected in the soil free-field at mid-depth. In experiments involving the liquefaction of large volumes of soil inside the container, the stiffness changes (and hence dynamic response) will change dramatically throughout the base shaking. A stiff chamber may lead to undesirable effects, as observed by Peiris (1999) who observed that liquefaction in a loose saturated sand model did not occur near the stiff end walls of the chamber. A chamber with no stiffness simply adds mass to the soil specimen, again changing its dynamic response. This poses a particular challenge for the ESB design.

The WES ESB was assembled using a urethane adhesive sealant (commonly used as a windshield sealant for cars) between the aluminium alloy rings, a material which was found to have good elastic properties and which bonded well to the metal and to itself. The new container has a low shear stiffness and a first mode around 16Hz, with second, third and fourth modes at 48, 79 and 109Hz respectively, Butler (1999). [A typical saturated specimen at 50g in the WES ESB will have a theoretical natural frequency around 92Hz, based on the small strain shear modulus.] The stiffness of the ESB was then investigated to assess its impact on the resulting combined soil-container response.

2.3 Dynamic response of the soil container and specimen

In his doctoral thesis, Butler (1999) has completed a thorough theoretical and experimental analysis of the dynamic response of the coupled soil-container system. At high g the soil and container act as a coupled system, where the lower stiffness of the container reduces the natural frequency (slightly) of the combined system compared to the soil column alone. However, provided the driving frequency is low relative to the natural frequency of the coupled system, Butler demonstrates that the displacement response of the system is unaffected compared to the soil acting independently, an ideal situation.

For higher driving frequencies, Butler concludes that it would be necessary to reconsider the elastic stiffness of the ESB container, and to tune the container to ensure that even with the expected level of degradation in the soil specimen, the coupled system did not deviate significantly from the condition of the soil column alone. This may be possible by adding mass to the rings of an initially stiffer ESB to reduce its first mode to the desired level, Butler (1999).

The liquefaction of a level sand bed has previously been the subject of other research. Experiments were conducted at many centrifuge centres under the VELACS project, Arulanandan and Scott (1994). The objective of the WES study is to investigate the onset of liquefaction under much higher initial effective overburden stresses.

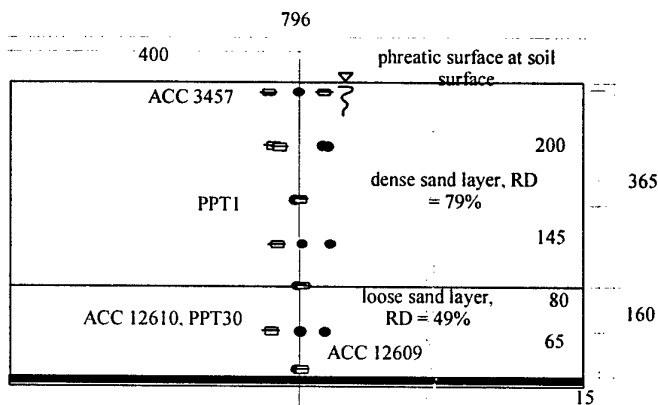


Figure 2.8 Cross-section through Model 3c

In the first major series of experiments using the WES earthquake actuator, the ESB container was filled with saturated sand, forming a level sand bed, Fig. 2.8. These are discussed in detail below. Instruments were placed at different depths to measure pore pressures and accelerations. The centrifuge was operated at 50g, creating a field equivalent of a site approximately 40m long by 15m wide by over 26m deep (for the deepest specimens). Surcharges and variations in the depth of the phreatic surface have been used to achieve higher effective overburden stresses, up to around 1000 KPa.

When the actuator is operated, the table is thrown backwards and forwards through a fixed amplitude of displacement, which is governed by the mechanical gearing of the system, as described above. In a perfect system, the peak amplitude would be reached in the first half cycle, but in practice tolerances in the mechanical design, and inertia of the specimen and container interfere with the theoretical output and the build-up to

a peak motion takes several cycles. Higher harmonics of the driving frequency are also often present.

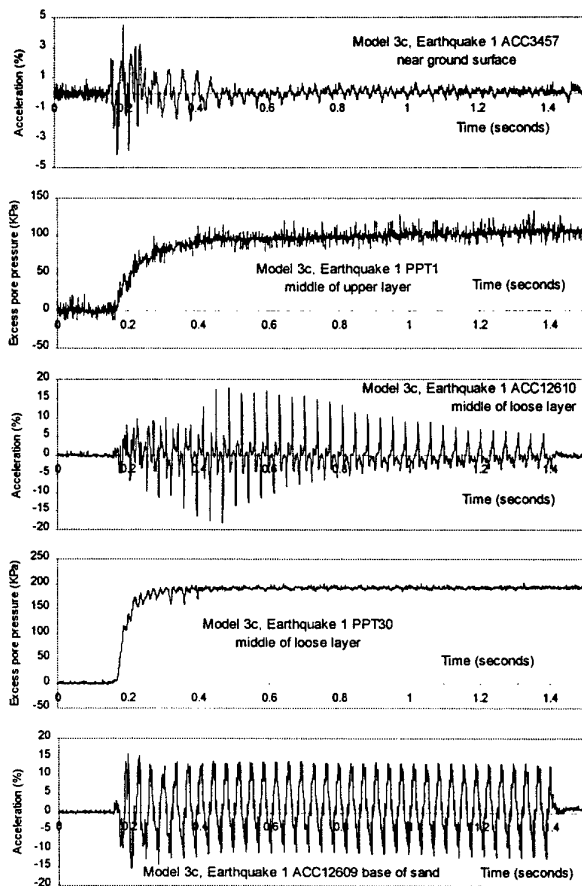


Figure 2.9 Time histories from Model 3c Earthquake 1

A schematic cross-section through a typical deep (525mm) model, Model 3c, is given in Figure 2.8. Typical earthquake time histories from Model 3c are illustrated in Figure 2.9, which shows the base shaking motion, motion at the middle of the loose layer, motion near the surface, as well as the excess pore pressure response at two depths in the specimen for the first earthquake, earthquake 1.

Butler's dynamic analysis of the container and specimen in his doctoral thesis (1999), has confirmed that the soil-structure system is responding satisfactorily without unacceptable boundary effects. In following sections of this paper, the data of earthquake response, excess pore pressures and accelerations are analysed in the context of conventional design methods for liquefaction assessment. However, the techniques of dynamic analysis applied to study the response of the whole system may also be applied with benefit to individual records within the soil specimen, providing additional valuable insights into the phenomenon of excess pore pressure development. The remainder of this section illustrates how this technique may be used to study the onset of liquefaction in detail.

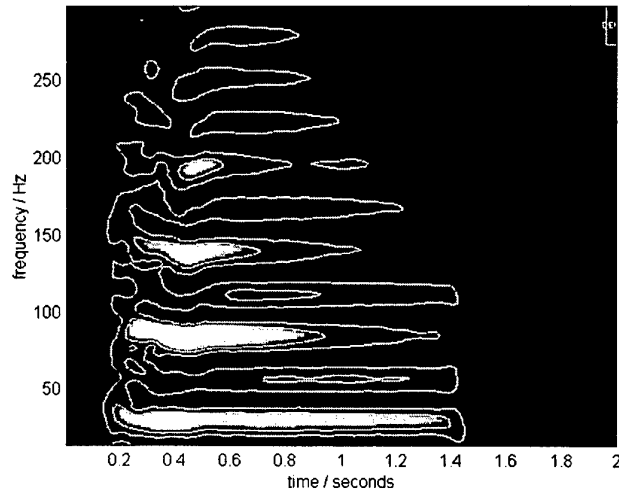


Figure 2.10 Harmonic wavelet plots of accelerometers 12610 (loose layer) Model 3c earthquake 1

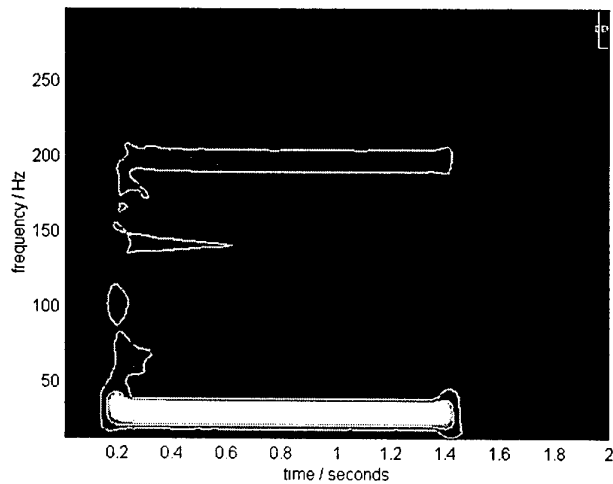


Figure 2.11 Harmonic wavelet plots of accelerometers 12609 (base of sand) Model 3c earthquake 1

Using harmonic wavelet analysis, time-frequency 'maps' can be generated from the time histories of acceleration recorded in the models. Newland and Butler have described the wavelet approach to the study of transient signals from centrifuge models in recent papers, Newland (1994, 1998), Newland and Butler (1998). Figures 2.10 and 2.11 show the time-frequency maps for ACC12610, in the middle of the liquefying loose layer compared with the base input motion ACC12609 throughout the earthquake.

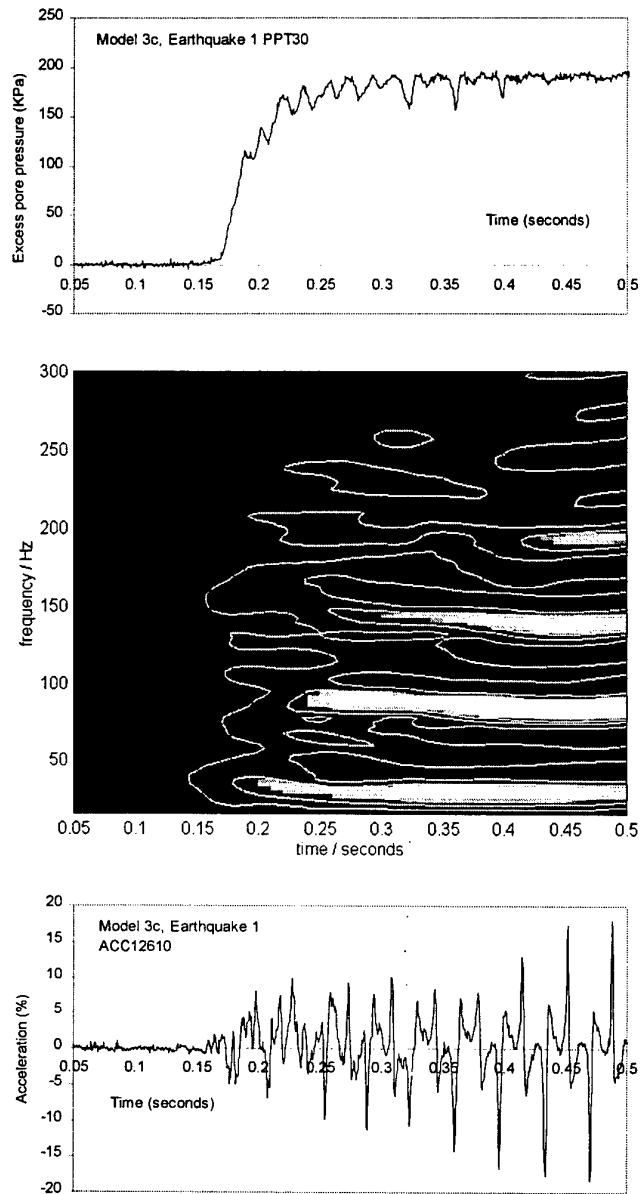


Figure 2.12 Early time response during onset of liquefaction, comparing a wavelet plot and time histories of acceleration with pore pressure, Model 3c earthquake 1

During the early stages of shaking, there is a rapid increase in excess pore pressure and consequent reduction in soil stiffness. This took place between about 0.17 and 0.27 seconds in earthquake 1. Time-frequency maps for this early stage is shown in Figure 2.12. In this plot, the excess pore pressure and the acceleration in the liquefying layer are also reproduced, to the same time scale, so that a direct comparison may be made. It is clear that during this period there is a reduction in at least one of the main resonance frequencies in the specimen, from around 90 to around 85 Hz. This frequency corresponds roughly to the third harmonic of the input

frequency (27 Hz) and also to the likely combined soil and container fundamental mode.

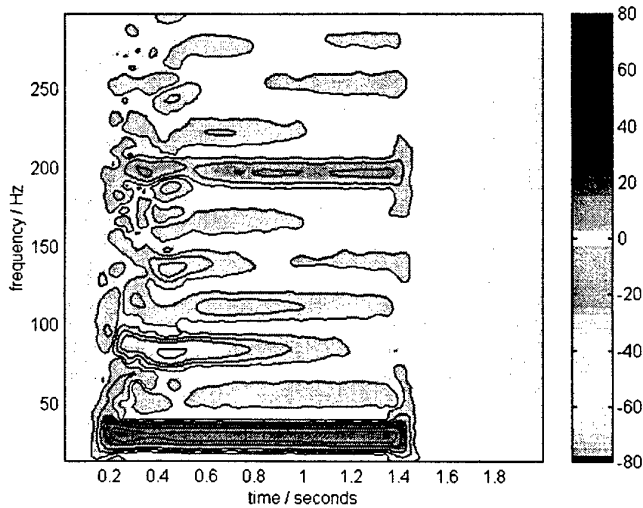


Figure 2.13 Differential plot of comparison between accelerometer 12609 (positive) and 12610 (negative) in Model 3c earthquake 1

In earthquake 1 and in later earthquakes a sharp rise in the energy at around 140 Hz took place almost exactly coincident with excess pore pressure reaching 100%. This is an interesting result which warrants further research. 140 Hz is near the fifth harmonic of the input shaking. Examination of the time histories in Figure 2.9 showed sharp spikes developing in the acceleration record as the soil around the accelerometer liquefies. The physical explanation of this is more complex. It may be associated with transient shock waves 'locking up' the soil instantaneously and then 'releasing' it again. If the shock wave was generated by the fundamental shaking motion of the specimen, then this would explain why the high frequency spike only occurs on each half cycle of base motion. Alternatively, it may be associated with a fracture type phenomenon as the soil liquefies and high frequency energy is generated.

Additional insights may be gained by subtracting the absolute values of two harmonic wavelet transforms to give a differential plot. This gives a comparison of the energy at different locations in the model. Figure 2.13 shows a differential plot for accelerometers 12609 and 12610 in Model 3c, earthquake 1. The intense band along the base of the figure shows that the input shaking energy is much greater at the base of the model than in the middle of the loose layer (ACC12610), as expected. However, energy at around 84Hz was amplified between the base of the sand bed and the middle of the loose layer, a small distance above. Here the absolute value of the differential is negative. This effect was transient in earthquake 1, decaying with time, but this pattern was different in subsequent earthquakes.

3 MODEL TEST CONFIGURATION AND INSTRUMENTATION

3.1 Outline of experiments

The model tests were designed to investigate the liquefaction of a loose saturated layer under varying effective overburden pressures. The principle aim of the experiments was to achieve an improved understanding of the K_σ factor in liquefaction analysis through centrifuge model tests of a level, saturated sand bed under strong base shaking. The objective of the series was to capture data of accelerations and excess pore pressures in a loose layer as excess pore pressures reach a condition of initial liquefaction under a range of different initial effective overburden stresses ranging from 1 tsf to 10 tsf. The experiments were conducted in the Equivalent Shear Beam (ESB) model container using the new earthquake actuator on the WES centrifuge, described above.

3.2 Summary of Model Test Series

Table 3.1 summarises the experiments conducted during 1998 and 1999. The models are grouped in series, where each series corresponds to a different target range of vertical effective overburden stress in the loose layer. In all cases, the bottom 160mm of the specimen was 'loose' and the upper portion 'medium-dense'. All models were shaken at 50g. Some models were overconsolidated by a factor of 2.5 prior to shaking (achieved by running the centrifuge upto 125g).

| Model series | Models in series | Effective overburden stress in loose layer | Depth of prototype (approx) | Depth of specimen | Notes |
|--------------|------------------|--|-----------------------------|-------------------|--|
| 1 | a | 1 tsf | 15 m | 300 mm | Ottawa sand |
| 2 | a, b, c, d, e, f | 1 tsf | 15 m | 300 mm | Nevada sand |
| 3 | a, b, c, d, e | 2 tsf | 26 m | 525 mm | Nevada sand |
| 4 | a, b, c, d | 3 – 5 tsf | 26 – 40 m | 525 mm | Nevada sand with lowered w.t. or surcharge |
| 5 | a, b, c, d | 7 – 10 tsf | 54 – 63 m | 525 mm | Nevada sand with lead surcharge |

Table 3.1 Summary of Model series

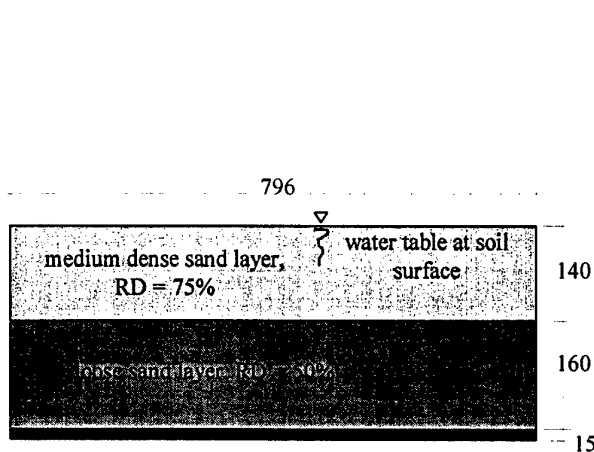
Table 3.2 provides further details on each experiment, including the densities achieved in the specimen, the date, the number of earthquake events and the actual initial vertical effective stress in the centre of the loose layer. Each centrifuge experiment generated a large body of data from instrumental records, from measurements made during construction and excavation, from photographs, video records and other sources.

| Model Code | WES CRC Ref. | Overall Depth (mm) | Density | σ_v' (tsf) | Date | OCR | Earth-quakes | Comments |
|------------|--------------|--------------------|------------------------|-------------------|----------|-----|--------------|--|
| 1a | 1 | 300 | 52% loose 70% dense | 1 | 4/12/97 | 1 | 2 | Ottawa sand, Cambridge ESB |
| 2a | 2 | 300 | 44% loose 83% dense | 1 | 20/2/98 | 1 | 3 | Nevada sand, Cambridge ESB |
| 2b | 5 | 300 | 50% loose 75% dense | 1 | 30/4/98 | 1 | 2 | Nevada sand, ESB #1 |
| 2c | 8 | 300 | 49% loose 74% dense | 1 | 6/6/98 | 1 | 5 | Nevada sand, ESB #1 |
| 2d | 9 | 300 | 50% loose 75% dense | 1 | 12/8/98 | 1 | 4 | Nevada sand, ESB #2 |
| 2e | 10 | 300 | 49% loose 73% dense | 1 | 26/8/98 | 2.5 | 4 | Nevada sand, ESB #1 |
| 2f | 14 | 300 | 50% loose 75% dense | 1 | 22/9/98 | 2.5 | 4 | Nevada sand, ESB #1 |
| 3a | 3 | 525 | 34% loose 73% dense | 2 | 30/3/98 | 1 | 2 | Nevada sand, Cambridge ESB |
| 3b | 6 | 525 | 49% loose 77% dense | 2 | 1/5/98 | 1 | 3 | Nevada sand, ESB #2, no data recovered from eq1 |
| 3c | 7 | 525 | 49% loose 79% dense | 2 | 5/5/98 | 1 | 3 | Nevada sand, ESB #2 |
| 3d | 11 | 525 | 54% loose 80% dense | 2 | 3/9/98 | 2.5 | 4 | Nevada sand, ESB #2 |
| 3e | 21 | | 50% loose 75% dense | | | 1 | | No useful data recovered |
| 4a | 12 | 525 | 49% loose 80% dense | 3 | 14/9/98 | 1 | 4 | Saturated to top of loose layer only. Nevada sand, ESB #1 |
| 4b | 13 | 525 | 56% loose 74% dense | 3 | 15/9/98 | 2.5 | 4 | Saturated to top of loose layer only. Nevada sand, ESB #2 |
| 4c | 17 | 525 | 50% loose 75% dense | 4.7 | 22/10/98 | 1 | 4 | Lead surcharge, Nevada sand, ESB #1 |
| 4d | 18 | 525 | 50% loose 68% dense | 4.7 | 4/11/98 | 2.5 | 4 | Lead surcharge, Nevada sand, ESB #1, model subject to further earthquakes to test new motor prior to disassembly |
| 5a | 15 | 525 | 51% loose 72% dense | 7.4 | 7/10/98 | 1 | 4 | Lead surcharge, Nevada sand, ESB #1 |
| 5b | 16 | 525 | 49% loose 76% dense | 7.4 | 14/10/98 | 2.5 | 4 | Lead surcharge, Nevada sand, ESB #1 |
| 5c | 19 | 525 | 52% loose 75% dense | 9.2 | 11/12/98 | 1 | 3 | Lead surcharge, Nevada sand, ESB #2 |
| 5d | 20 | 525 | 57% loose 80% dense | 9.2 | 17/2/99 | 1 | 1 | Lead surcharge, Nevada sand, ESB #2 |

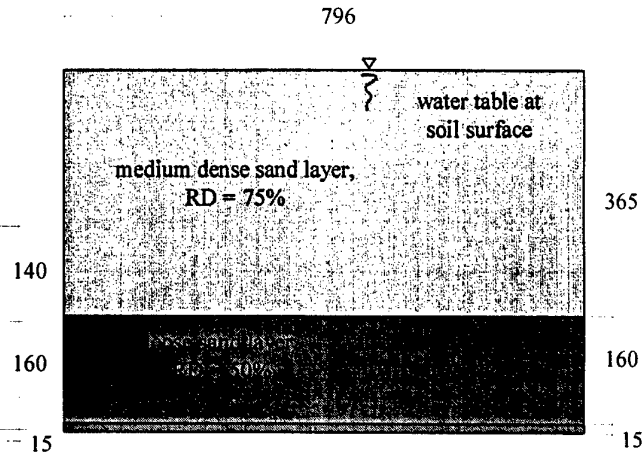
Table 3.2 Summary of experiments

The objective for the upper portion of the specimen was to create a medium dense ($D_r = 75\%$) sand, and for the lower layer a target relative density of around 50%. The

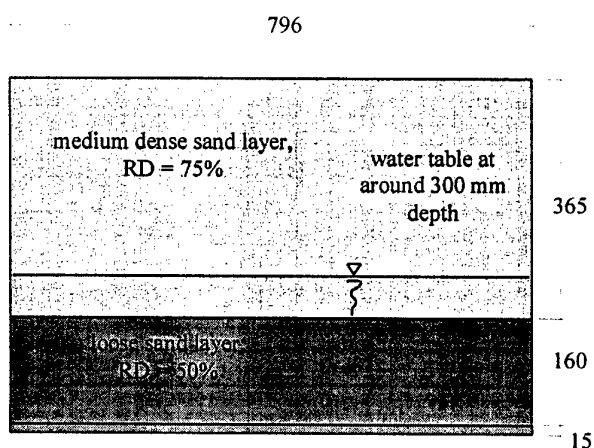
depth of the upper portion, water table and magnitude of surcharge were calculated to ensure the target effective overburden pressure was achieved at mid-height in the loose layer. The first model was constructed with Ottawa sand (Model 1a) but all subsequent models (which included repeats of earlier experiments) used Nevada sand (Model series 2, 3 etc).



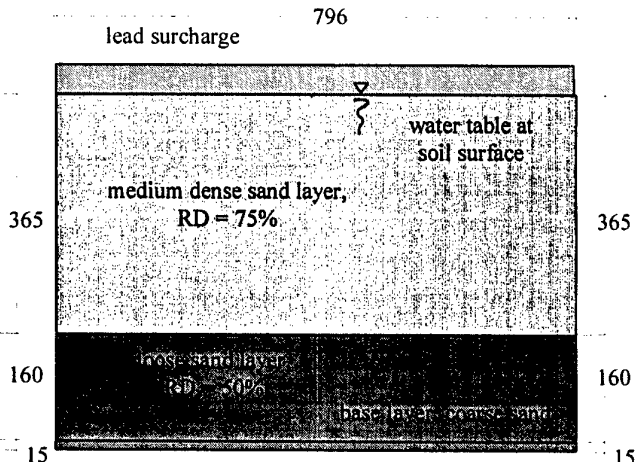
Typical cross section through Model series 1 and 2



Typical cross section through Model series 3



Typical cross section through Models 4a, 4b



Typical cross section through Models 4c, 4d and 5

The importance of the target elevation in the middle of the loose layer was that a fixed volume of sand of similar relative density lay below.

The specimens were all 300mm wide, between the vertical side walls of the ESB. The side walls comprised smooth glass plates mounted against the aluminium rings, providing a sheer low friction interface. (This was in contrast to the end walls, which comprised roughened steel 'shear sheets', described above.) On the base, slotted plates were used to assist the saturation process by distributing fluid over the base of the model. Coarse sand was used to fill the slots, providing a filter and creating high friction interface between the specimen and the base of the container.

As the prototype depth was increased, the options were to shake the models at a higher g level, to depress the water table or phreatic surface, or to use surcharging to

achieve the target overburden. It was determined that the models should all be shaken at 50g, and that surcharging would be adopted to reach the required stress levels. In the Model 4 series, two models used a depressed phreatic surface and two used surcharging. In the Model 5 series, the prototype depth was too great to be achieved without surcharging. The surcharge comprised lead strips laid lengthwise along the surface of the specimen, with additional lead plate on top where necessary.

3.3 Materials

The materials used in the model were characterised by standard laboratory tests to determine parameters such as dry density and gradation. With the exception of Model 1a, all models were constructed using Nevada sand and saturated with a glycerine-water solution. Tables 3.3, 3.4 and 3.5 present key material parameters for Ottawa sand, Nevada sand and glycerine-water solution respectively.

| | |
|--------------------|-------------------|
| Specific gravity | 2.68 |
| Maximum void ratio | 0.7633 |
| Minimum void ratio | 0.4762 |
| D ₅₀ | 0.12 mm (approx) |
| D ₁₀ | 0.075 mm (approx) |

Table 3.3 Ottawa Sand specification (from VELACS)

| | |
|--------------------|---------------------------|
| Specific gravity | 2.64 |
| Maximum void ratio | 0.757 (density 93.8 pcf) |
| Minimum void ratio | 0.516 (density 108.7 pcf) |
| D ₅₀ | 0.18 mm (approx) |
| D ₁₀ | 0.11 mm (approx) |

Table 3.4 Nevada Sand specification (as measured)

The pore fluid comprised a mixture of glycerine and water, 80% by weight for experiments conducted at 50g. Measurements of the viscosity of glycerine-water mixes at a range of temperatures and proportions show that the viscosity is sensitive to both parameters, Fig 3.1, Steedman (1999).

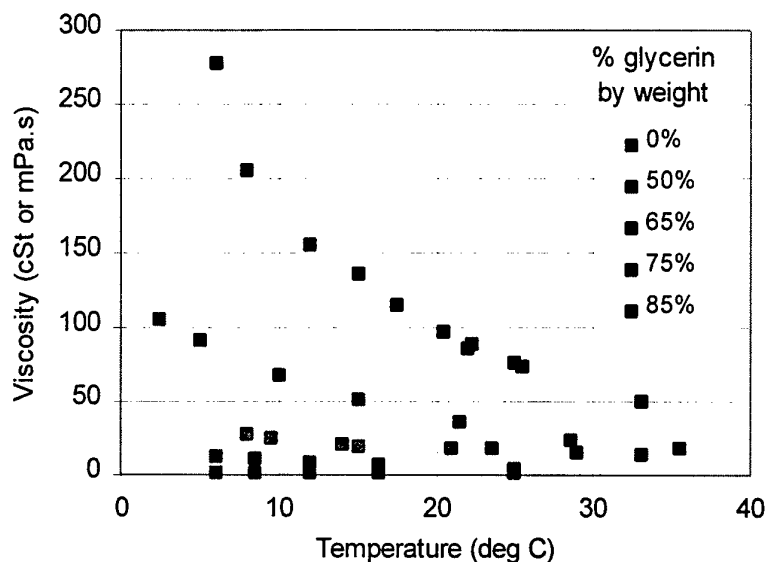


Figure 3.1

The density of a glycerine-water mix was calculated from:

$$\rho_m = \rho_g(m_g + m_w) / (m_g + \rho_g m_w)$$

where ρ_m is the density of the mix, ρ_g is the density of glycerine, m_g is the mass of glycerine, and m_w is the mass of water. Table 3.5 summarises the properties of the glycerine-water solution used as the pore fluid.

| | |
|------------------|-------------------------------------|
| Density | 1200 kg/m ³ |
| Viscosity | 50 cs |
| Specific Gravity | 1.26 |
| Composition | 80% glycerine-water mix (by weight) |

Table 3.5 Specification for pore fluid (as measured)

The models were poured dry from a hopper and saturated under vacuum, or occasionally under gravity. Instrumentation was placed in the model as it was being constructed.

3.4 Instrumentation layout

Each specimen was instrumented with accelerometers and pore pressure transducers. Details of the exact locations of all instruments are contained in the factual report prepared for each experiment. Figs. 3.2, 3.3, and 3.4 show the typical locations and type of instrumentation in three models, representative of the Model 2, Model 3 and Model 5 series.

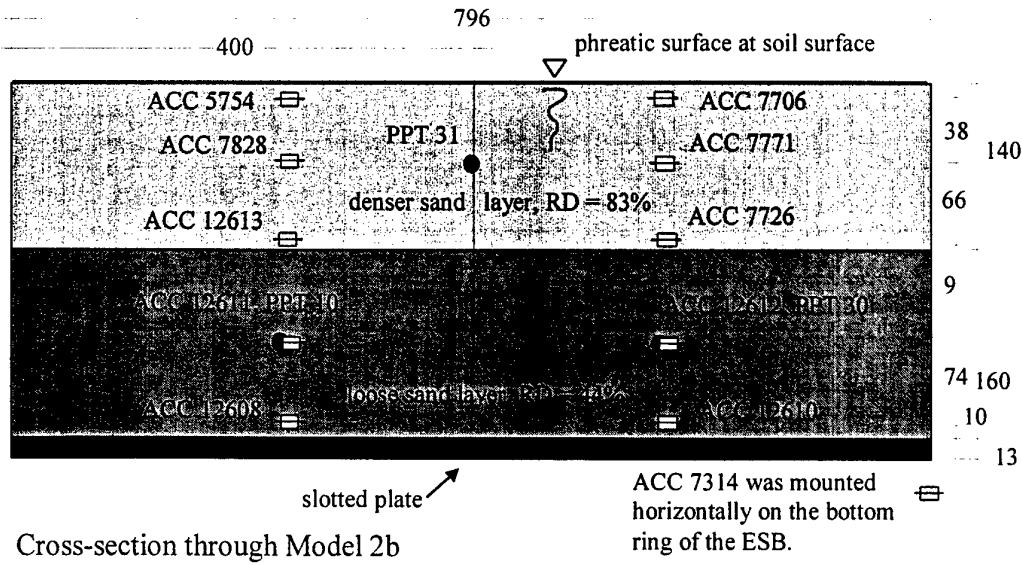


Figure 3.2 Instrumentation typical of Model 2 series

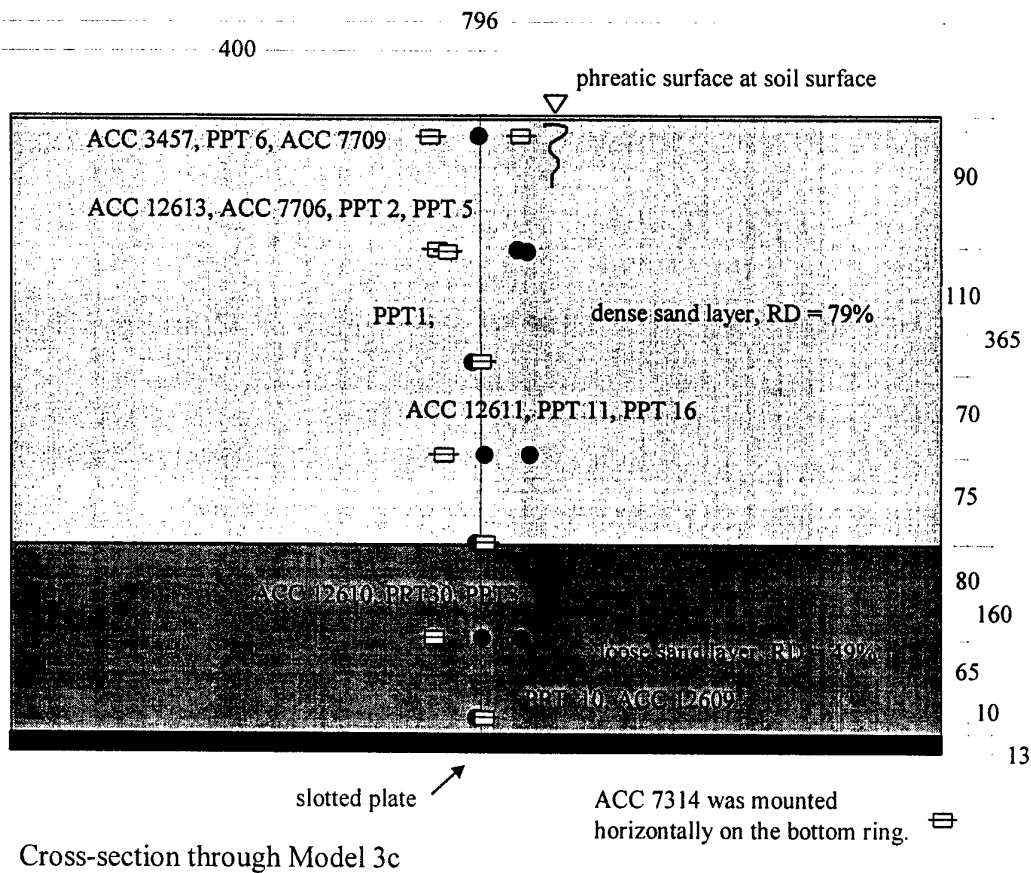


Figure 3.3 Instrumentation layout typical of Model 3 series

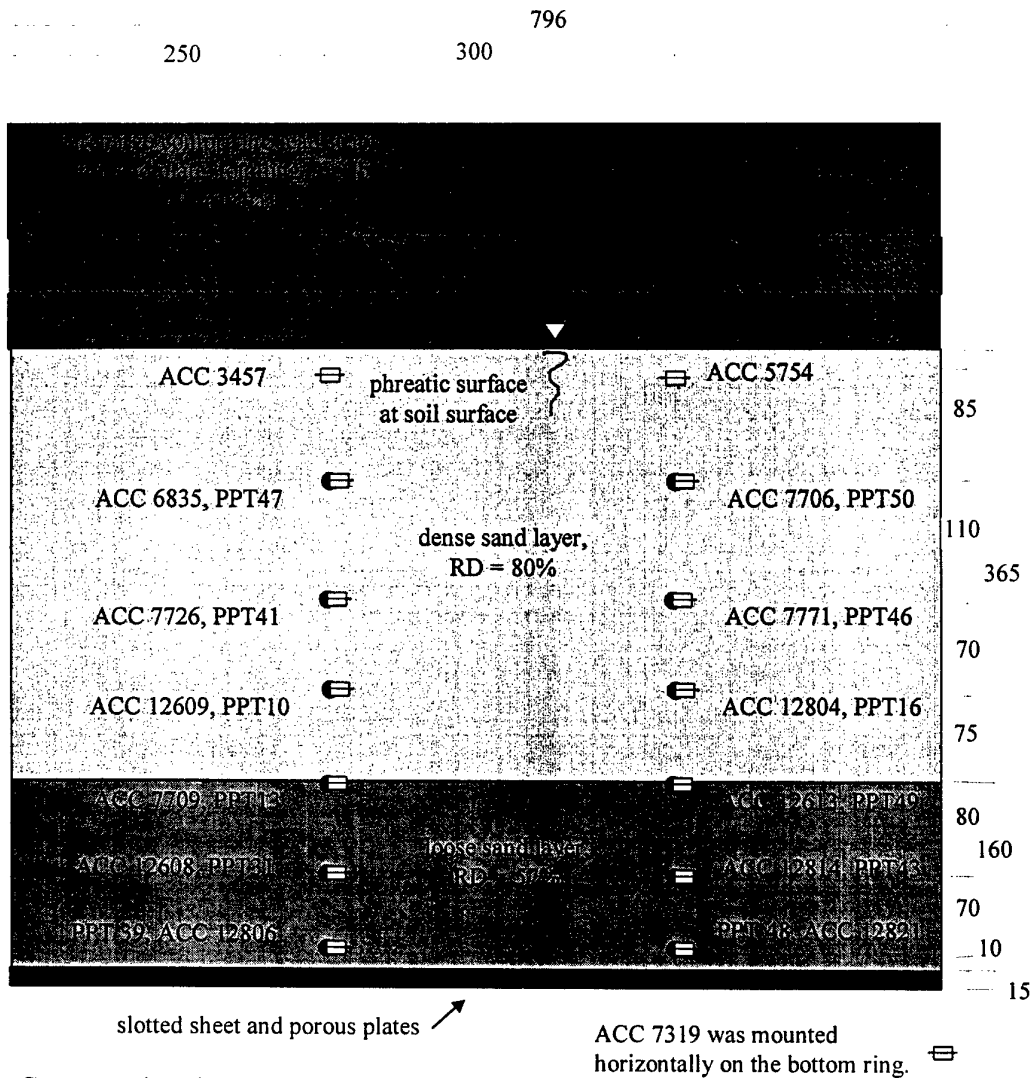


Figure 3.4 Instrumentation typical of Model series 4 and 5

The accelerometers used in the models were piezoelectric capacitive devices manufactured by D J Birchall (UK) and Endevco (US). In the above figures, the Birchall devices are identified by a four digit reference number; the Endevco devices are numbered 12xxx. Typical calibrations for the Birchall devices are around 0.12 mV/g. The Endevco accelerometers are around half of this sensitivity, with calibrations typically around 0.05 mV/g. Cables from the devices were routed to the side walls of the model chamber and up the glass sides, Fig. 3.5.

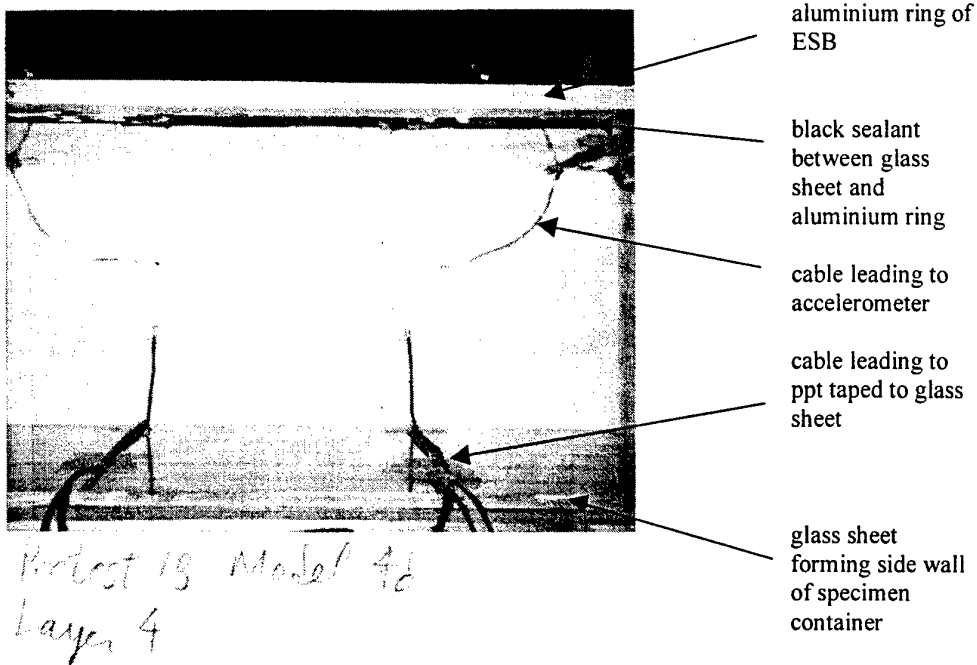


Figure 3.5 Polaroid photo of instrumentation placement at layer 4 in Model 4d

Fig. 3.5 also shows clearly the side wall arrangement used in the experiments, with glass sheets mounted inside the aluminium rings of the ESB. A soft elastic sealing compound was used to fill voids between the glass and the aluminium, shown in black in the photograph.

Vibrations of the cables was minimised by bundling them together and securing them to gantries. Amplifiers mounted in a junction box on the vertical support wall of the shaker converted the input signals to voltages.

The pore pressure transducers used in the experiments were manufactured by Druck, and are widely used in centrifuge modelling. Typical calibrations depend on the range of the device, and vary from around 0.17 mV/V/psi for a 5 bar device to 0.036 mV/V/psi for a 35 bar ppt. Using amplifiers in the junction boxes, these signals were conditioned and stored locally on an on-board computer before transmitting them through the slip rings to the data logging system in the control room.

4 ANALYSIS AND INTERPRETATION OF EARTHQUAKE MODEL TEST DATA

4.1 *State-of-practice for liquefaction assessment*

The established method of assessment of liquefaction resistance of a soil layer or column is to conduct field (in-situ) investigations and to correlate measurements of standard penetration resistance, cone resistance or other parameters with field observations. Estimation of the cyclic stress ratio (CSR) and the cyclic resistance ratio (CRR) are then used to assess the likelihood of liquefaction. These are defined as the seismic demand on the soil and the capacity of the soil to resist liquefaction respectively, Youd and Idriss (1997). Assessment of the CRR is subject to corrections such as those proposed by Seed (1983) to account for factors such as depth (K_σ) and high initial static shear stress (K_α) where the method is extended beyond the original data-set. Because of the absence of case history data against which comparisons could be made, these factors have had to be developed using laboratory test data.

The present state-of-practice for determining the performance of soils that undergo earthquake-induced shear-strain and consequently pore water pressure buildup in saturated soils is to determine if a soil will or will not liquefy. The performance and safety of structures are based on rigid sliding-block/slices limit-equilibrium methods to determine slip-plane stability and deformation using residual strengths in the case of liquefaction.

In-situ methods such as Standard Penetration Test (SPT), Cone Penetration Test and shear wave velocity measurements are used to define the triggering of liquefaction. The potential for liquefaction relies on empirical correlation between the penetration resistance and the performance of soil deposits in past earthquakes (Seed, 1979). The database on triggering liquefaction is based on data from level ground where surface evidence occurred. Soil conditions were shallow at overburden pressures less than about 95.8 kPa (about 4.6m of depth). The data base is normalized to an earthquake of magnitude 7.5. Corrections for other earthquake magnitudes have to be made (Seed & Harder, 1990, NCEER, 1996).

To extend the database to depths representative of foundation soils under dams requires the use of correction factors (Seed & Harder, 1990) for the effects of overburden pressure and initial static shear-stress. Correction for high overburden, K_σ , is based on laboratory test results of the ratio of cyclic-shear-stress, CSS, to cause liquefaction at an overburden effective-stress state, σ'_o , to that at a $\sigma'_o = 95.8$ kPa. Correction for initial static shear-stress, K_α , is based on the ratio of CSS to cause liquefaction with initial static shear-stress applied to that at no initial static shear-stress.

A factor of safety, FSL, against the occurrence of liquefaction, defined as 100 percent pore water pressure, can be calculated as:

$$FSL = f [(N_1)_{60}] K_m K_\sigma K_\alpha / \tau_{eq}$$

Where $(N_1)_{60}$ is from SPT relations, K_m is earthquake magnitude or duration correction factor and τ_{eq} is a percentage of peak earthquake induced shear stress.

The FSL can be related to percent excess pore water pressure.

The correction factor $K\sigma$ has a large influence for dam foundations. It can reduce the CSS to cause liquefaction to about 45 percent of its in-situ value at pressures about 670 KPa that would exist beneath an embankment dam about 30.5m high.

Alternatively, if SPT criteria were being derived for remedial treatment of this dam to limit the potential level of earthquake generated pore water pressures, the $K\sigma$ factor would cause an increase of more than double in the required penetration values to be measured in the field. Clearly, the correction factor can have a major impact on the potential for triggering liquefaction or the excess residual pore water pressures and on the cost of remediation.

The correction factor $K\alpha$ can also contribute significantly to the reduction of the in-situ strength. However, for relative densities above 45-50 percent, $K\alpha$ can have a positive effect on the in-situ strength. The $K\sigma$ relationships are not well defined.

In application of the state-of-practice, the following assumptions are made inherently: (1) the soil is always undrained, (2) liquefaction occurs instantaneously and the soil shear strength jumps to residual state, (3) residual strength is constant with monotonic loading, (4) liquefaction is independent of soil zone thickness, permeability, or boundary conditions, (5) liquefaction is independent of when the earthquake peak energy arrives, (6) behavior of the liquefied soil and its resultant effects on a dam are independent of the soil zone thickness, permeability, and boundary conditions, (7) dam stability and deformation are controlled by slip-planes independent of the liquefied soil zone thickness and behavior, and (8) non-liquefied soil at a site is unaffected by the earthquake. Field behavior, numerical analyses, and physical model tests show that these assumptions are invalid.

4.2 *Research problem*

Current studies for more thorough evaluation of liquefaction and for remediation design and analysis have shown serious limitations in the state-of-practice. The state-of-practice can force costly excessive remediations to be undertaken when possibly no action is required, but it can also lead to unsafe conclusions in other cases.

Significant progress is being made in the development of numerical methods for analysis of liquefaction and the consequences. However, the engineering profession will most likely always use empirical correlation (Seed's or others) of in-situ measurements versus potential liquefaction, pore water pressure generation and earthquake response. Every time a site is evaluated for a seismic design or potentially liquefiable soil is improved and a dam remediated, in-situ measurements will be made. A value/range of in-situ measurement to achieve will be specified for a construction/remediation contractor. Some in-situ measure will be used to judge soil conditions/improvement and seismic safety of a dam or site. Therefore, improvement in the current state-of-practice and the empirical correlations between in-situ measures and performance of soil deposits has to be made.

Current studies of the seismically-induced deformation behavior of dams indicate that as soils are progressing toward liquefaction (pore water pressure is increasing and

shear strain is occurring) significant deformations of the structure can occur. Failure (damaging levels of deformation) can develop significantly before the complete initial liquefaction stage (100 percent pore water pressure ratio) is reached. Depending on specific conditions involving the location, depth and extent of liquefying soil and the driving forces, a structure may fail at only 50 percent strength reduction. In this case, remediation to assure safe performance is required to prevent serious damage significantly before an initial liquefaction condition and a residual strength stage are arrived at in the soil.

The problems in the current state-of-practice stem mainly from the fact that for the sites that have liquefied and constitute the empirical basis for analysis, the following are not known: (1) the exact and complete soil conditions and profiles, (2) the real behavior that occurred in the soils during and after the earthquakes or the various influences on the behavior, (3) the development of pore pressures or strains in the assumed non-liquefied soils (used in comparison to liquefied soils) which may have changed state during the earthquakes, and (4) whether artificial and possibly incorrect conditions in laboratory testing may have led to conclusions not totally applicable to the field behavior.

Improved definition and physical evidence is therefore needed of the processes and mechanisms involved as a soil progresses to liquefaction and residual strength. This is needed to allow refined analyses for dam safety and more cost-effective and safe remediation design and analysis. Because various assumptions can be made coupled with methodologies and numerical analyses that can give solutions or answers to almost anything, the reality-check of solutions must come from field or equivalent-field data of behavior under well known and defined conditions.

The earthquake response database needs to be expanded with more complete data to provide: (1) the necessary advance in the state-of-practice, (2) a basis for modification and improvement of current methodology and assumptions, and (3) definition of the physical processes and mechanisms involved in the liquefaction process and resultant effects on dam behavior. This would also provide the fundamentals and basis for development of new methodology and analyses. New methodologies have to be based on correct mechanisms and processes.

Current specific needs for more thorough earthquake engineering analyses can be identified from examination of the last two decades of experience in seismic evaluation of embankment dams and the serious limitations that arise when remediation design is attempted. Studies involving liquefaction, stability, and seismic-induced deformation behavior of dams raise serious questions that impact the safe performance and needs for remediation (e.g., Ledbetter and Finn, 1993, Ledbetter, et. al., 1994, Finn and Ledbetter, 1991, Finn, et. al., 1991 and 1994, Vaid and Chern, 1985, Vaid and Thomas, 1994, Bryne and Harder, 1991). For example, Vaid and Thomas (1994) demonstrated that $K\sigma$ for specific sand types may be substantially less (more than a factor of 2) than suggested by Seed and Harder. Pillai and Byrne (1994) showed for the foundation materials of Duncan Dam, a $K\sigma$ of 0.6 compared with 0.4 from the Seed and Harder relation. This made a difference between recommending remediation and no remediation. There is a large spread of $K\sigma$ relations and data by various researchers that can influence whether to remediate a dam at costs in the tens of millions of dollars or not remediate.

For the past thirty years, research has primarily concentrated on the triggering of liquefaction of soils both in the laboratory and in field sites. A significant database has resulted of very important and necessary information concerning the stress-state triggering of liquefaction, cyclic load stress-ratio and the dynamic properties of soils. Newmark, 1965, stressed that what counted was whether the deformations that a dam suffered during an earthquake were tolerable or not. Peck, 1992, stated that of all measures of safety, the most directly applicable results are the anticipated deformations.

Due to the lack of knowledge and experience involving the behavior of liquefiable soils under field conditions, simplifying assumptions are forced to be made for the critical safety of dams, concerning behavior. Possible significant controlling influences such as permeability, boundary layers and pore water pressure dissipation and migration must be disregarded.

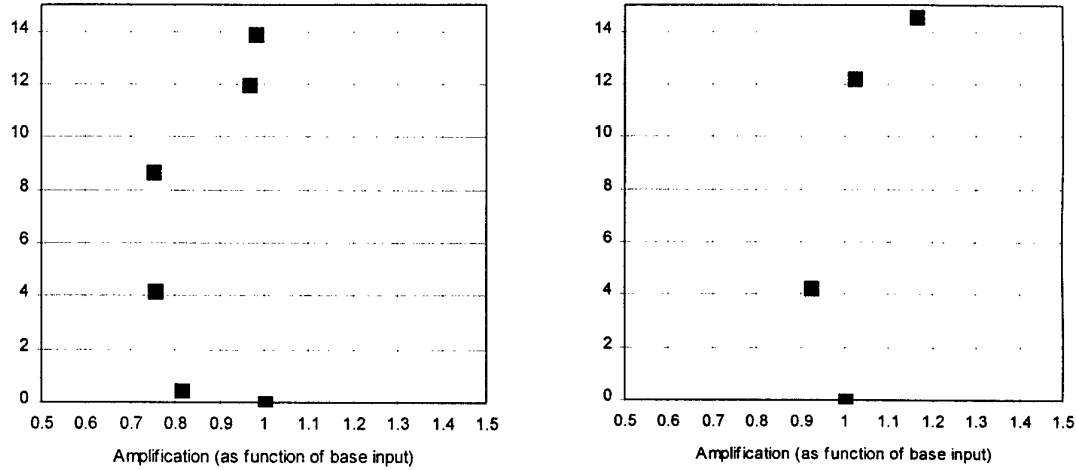
Some specific needs are: (1) well defined and complete shear stress-strain response curves for earthquake loading including the residual strength portion, (2) strains within a problem soil mass, (3) effects of soil zone thickness, permeability, and boundary conditions, (4) influence of adjacent soil materials and of their permeabilities, (5) dissipation and movement of excess residual pore pressure both during and after an earthquake, (6) redistribution of stresses as a soil is losing strength, (7) interaction of remediation materials and adjacent soil, (8) dynamic response of remediation materials and of remediated zones, (9) improved $K\sigma$ and $K\alpha$ factors for the field evaluation of remediation achievement and for improved first estimates of liquefaction potential, (10) effects of strong aftershocks and (11) dam internal behavior and failure mechanisms in response to earthquake loading and strength degradation.

The experimental investigation using the Army centrifuge at WES has been used to address these issues as it has provided, for the first time, a substantial body of data of the behavior of liquefying soil deposits under a wide range of initial effective confining stresses. In the following sections, the method by which the data has been analysed is presented. Although the experiments adopted a target effective confining stress within a loose layer at some depth, instrumentation at other depths also provided valuable information on the degradation of the soil column. In some cases, upper layers were clearly affected by the generation of excess pore pressure in layers below. This is typical of field behavior, although not of laboratory element tests. The first stage in the experiment analysis was to develop the method by which $K\sigma$ could be calculated within the soil column.

4.3 *Calculation of $K\sigma$ from measurements made in a soil column*

The stress history at the location of each transducer was calculated using a time history of acceleration. One accelerometer record was selected based on the quality of its signal and its location. Generally the device was located on the bottom ring of the ESB, but occasionally the accelerometer at the base of the sand specimen was used instead. In some cases, where amplification was considered significant, an amplification analysis was carried out by examining the peak acceleration at different elevations in the model, based on the very early cycles of shaking before significant

degradation had taken place. The mean of positive and negative cycles was used, and commonly high frequency spikes were removed by smoothing where these were considered to be unrepresentative of the character of the motion. Plotting amplification as a function of the base input motion revealed that generally the amplification was around 1, Fig 4.1.



Note: amplification calculated at each elevation as the mean of the positive and negative peak values during the second cycle of shaking, between 0.28 and 0.32 seconds. The mean of both accelerometers at each elevation was then used, with the exception of ACC 12610 (unreliable) and on the base, where only one accelerometer was available.

Note: amplification calculated at each elevation as the mean of the positive and negative peak values during the second cycle of shaking, between 0.95 and 1.1 seconds. The mean of both accelerometers at each elevation was then used, with the exception of the near surface, the middle of the loose layer and on the base, where only one accelerometer was available.

Model 2b, amplification during second cycle of base shaking

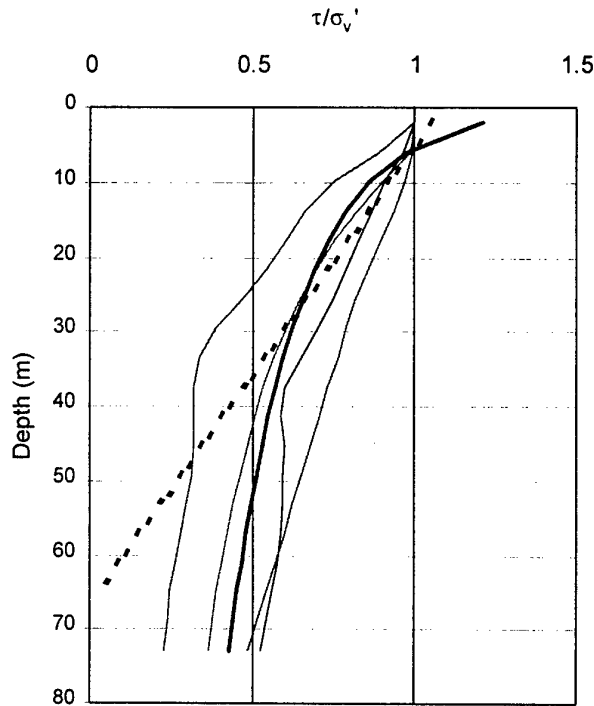
Model 2c, amplification during early cycles of shaking

Figure 4.1 Amplification during early cycles of shaking for two models

The cyclic stress ratio (CSR) at any depth was calculated using the relationship originally proposed by Seed and Idriss (1971) and developed by Ishihara (1996),

$$CSR = \frac{\tau_{av}}{\sigma'_v} = 0.65 \frac{a_{max}}{g} r_d \frac{\sigma_v}{\sigma'_v}$$

where a_{max} is the peak acceleration at the ground surface and τ_{av} is the shear stress on a horizontal plane.



Comparison between 'effective' stress ratios calculated for deep soil columns using data from SHAKE-7 analyses of two field earthquakes (Loma Prieta and El Centro), one artificial earthquake (Folsom Record B) and one centrifuge earthquake (Model 3c earthquake 1). Soil column was assumed to be all sand, shear modulus and damping properties set to 'average' values. The water table assumed to be at the surface. Graphs also show 'effective' stress ratio calculated using ground surface acceleration based on two alternative reduction factors with depth,
 $rd = 1 - 0.015z$, and
 $rd = 1.25 - 0.2 \ln(z)$

Figure 4.2 Output from SHAKE computations of the response of a soil column to four different earthquake motions

There is a wide range of reduction factors rd proposed in the literature. For this study, a mean rd was developed based on analyses using SHAKE of soil columns similar to those constructed in the centrifuge experiments. Figure 4.2 shows the response of a deep saturated soil column to two field earthquakes (Loma Prieta, Hollister Airport and El Centro), one artificial time history (Folsom Dam Record B) and a centrifuge earthquake base input motion (Model 3c, earthquake 1). The SHAKE output is plotted in terms of stress ratio against depth, and compared with

a) a simple linear function for rd (Iwasaki et al. (1978),

$$rd = 1 - 0.015 z \quad (z \text{ in metres}),$$

recommended as suitable for depths up to 25m, and

b) a log function proposed based on this study,

$$rd = 1.25 - \ln z \quad (z \text{ in metres}),$$

which fits the data well for all depths greater than around 2m.

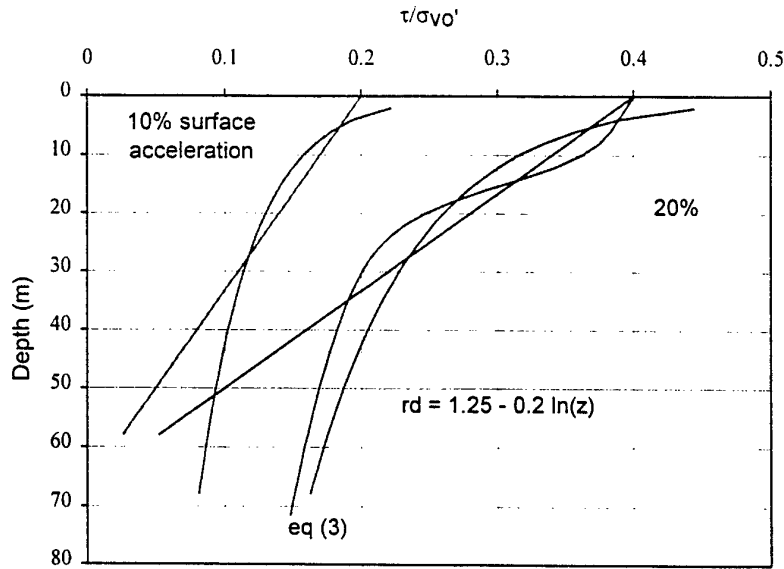


Figure 4.3 Shear stress ratio required at different depths to generate 10 – 20% ground surface acceleration, based on $rd = 1 - 0.015z$, $rd = 1.25 - 0.2 \ln(z)$ and Youd and Idriss

Figure 4.3 shows a comparison between these two functions and the output based on a more complex function proposed by Youd and Idriss (1997), equation (3), for ground surface accelerations of 10% and 20%g.

The true character of stress ratio with depth is significantly affected by the development of excess pore pressure in the soil column. In practice, the ground surface acceleration time history will be distorted by the liquefaction in the soil strata beneath, which often isolates the surface from the underlying motion. In this study the base input motion was used, and scaled using an amplification factor derived from the actual profile of amplification observed in the specimen. The stress history at any depth was then computed following equation (1).

Following this approach, the full dataset was processed. Appendix A presents the data in detail.

4.4 SHAKE analysis of soil column

SHAKE may also be used for the prediction of time histories of output acceleration at different levels in the soil column. However, the onset of liquefaction has a dramatic effect on the acceleration in the upper part of the soil column, and this is not reflected in the SHAKE calculation. Fig. 4.4 shows the output motion for layer 1 (surface) compared with the actual surface motion and input base motion for Model 3c, earthquake 1 (see also Fig. 2.9).

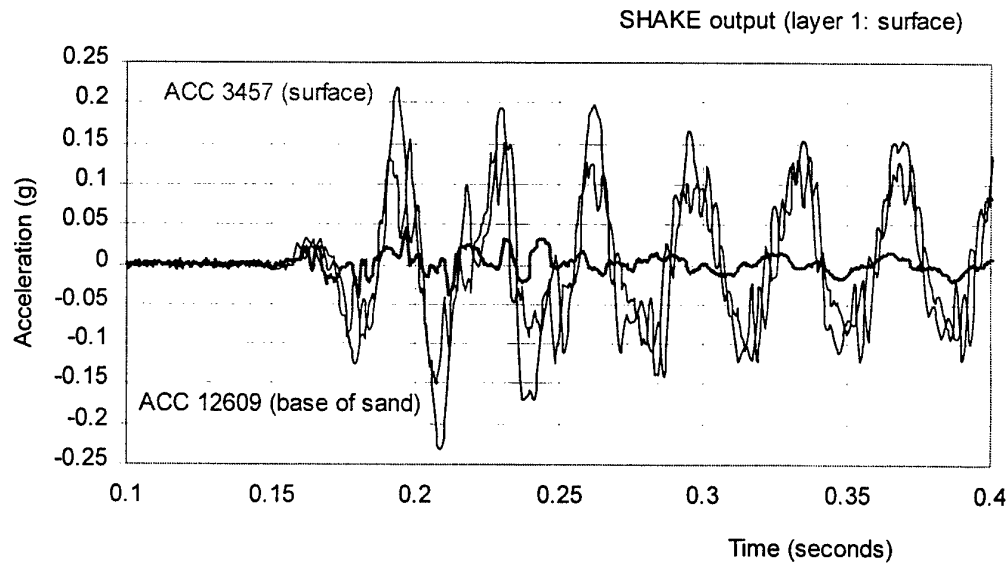


Figure 4.4 Comparison between actual surface motion and SHAKE calculation in liquefied specimen, Model 3c, eq1

The SHAKE soil model used in the calculation was in 20 layers, with upper bound values of soil stiffness and damping. The soil column was around 26 m deep, with the water table at the ground surface. The output confirms that estimates of amplification close to 1 are realistic for the purposes of the analysis.

4.5 Comparison with published Magnitude Scaling Factors

Many excess pore pressure records showed a cyclic response during pore pressure buildup, and the peak pore pressure would reach the ultimate limiting value significantly before the residual. Typical data from Model 3c, earthquake 1 is shown in Figure 4.5. The time at which the residual pore pressure reached the limiting value was adopted as the most consistent and reliable definition of the onset of initial liquefaction.

Using the period associated with the dominant frequency of shaking, the number of 'cycles' to reach liquefaction was calculated based on the time and the dominant period of earth shaking. Table 4.1 illustrates the output.

| Actual depth (mm) | Prototype depth (m) | Static pore pressure at 50g (KPa) | Depth fluid on surface (m) | Total vertical stress, σ_v (KPa) | Effective vertical stress, σ'_v (KPa) |
|---|---|--|---------------------------------------|--|---|
| 439 | 21.95 | 263 | 0.391 | 457 | 194 |
| Maximum cyclic stress ratio (raw) | Maximum cyclic stress ratio (smoothed) | Cyclic stress ratio (CSR) τ/σ'_v | Effective vertical stress (tsf) | Onset of initial liquefaction (seconds) | Number of cycles equivalent (N) |
| 0.232 | 0.225 | 0.146 | 2.1 | 0.308 | 4.27 |
| Data for : G level | Model 3c Unit weight (dense) | PPT 30 Unit weight (loose) | Fluid unit weight | Earthquake start (seconds) | Frequency (Hz) |
| 50 g | 20.7 KN/m ³ | 20.2 KN/m ³ | 11.77 KN/m ³ | 0.15 | 27 |

Table 4.1 Base data and calculations of stress ratio and number of cycles to liquefaction for PPT30, Model 3c, earthquake 1 (refer also to Figure 4.4)

The base shaking motion shown in Figure 4.5 was selected to simplify the derivation of a representative K_σ value. The selection of Magnitude Scaling Factors was based on data reproduced by Youd and Idriss (1997). It was found that the original Seed and Idriss MSF values generate a 'flat' curve represented by the function $F = 5.24 N^{-0.61}$. Proposals by Ambraseys can be represented by a relatively steep curve matched by the function $F = 3.48 e^{-0.08 N}$. A more recent proposal by Idriss (Youd and Idriss, Table 3) yields a steeper curve, represented by the function $F = 3.47 N^{-0.45}$.

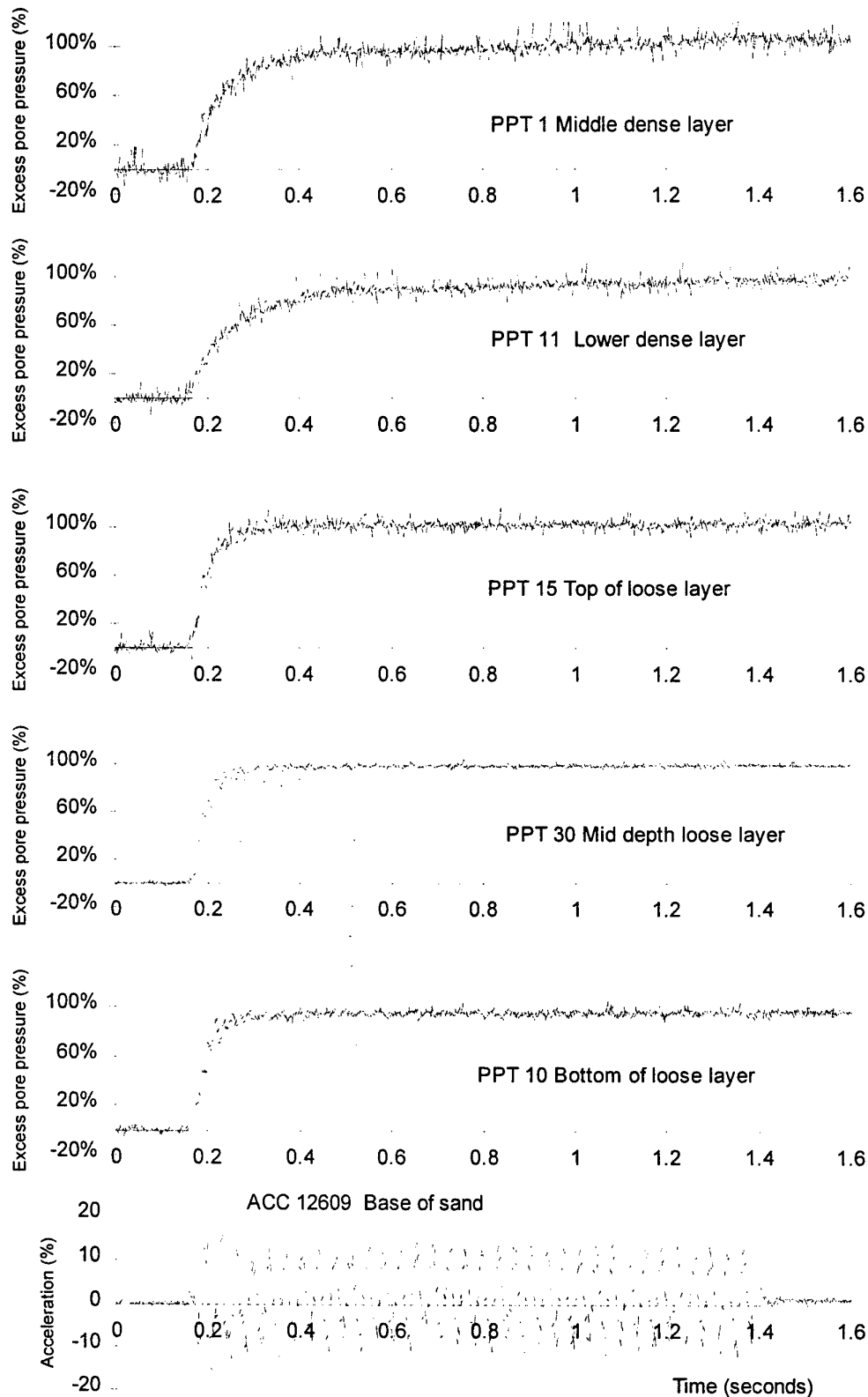


Figure 4.5 Development of excess pore pressures in Model 3c, earthquake 1

Figures 4.6, 4.7 and 4.8 show the families of curves generated by these three functions compared with the centrifuge data of normally consolidated 50% RD, first earthquake

specimens. The Idriss MSF factors were selected as most appropriate (of the three choices), although a slightly flatter curve could have been chosen to match the data more closely. Using the Idriss curve function, the least squares best fit curve to the data at 1 tsf was found, and this is shown in Figure 4.8.

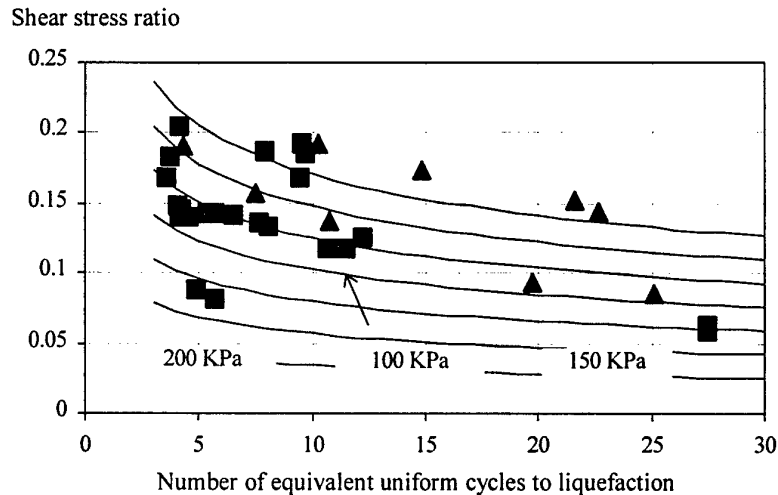


Figure 4.6 Comparison between all data and the shape of the liquefaction curves predicted using the MSFs of Seed & Idriss (data only reaching 90% excess pore pressure or greater)

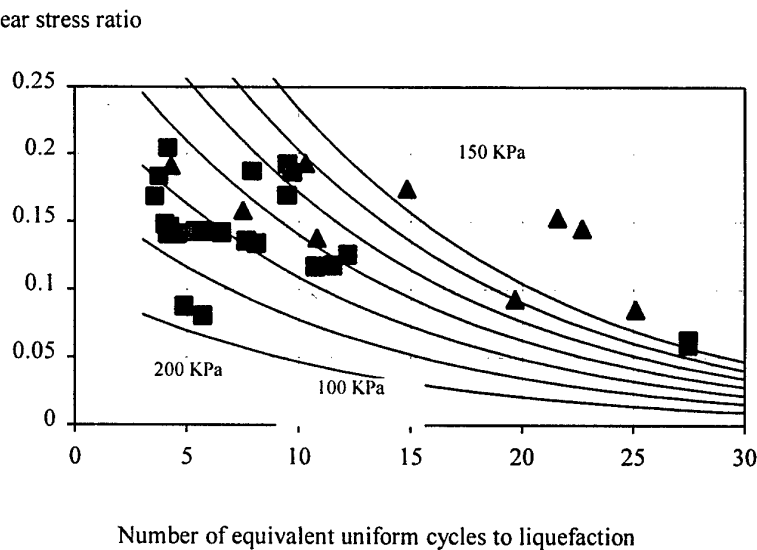


Figure 4.7 Comparison between all data and the shape of the liquefaction curves predicted using the MSFs by Ambraseys

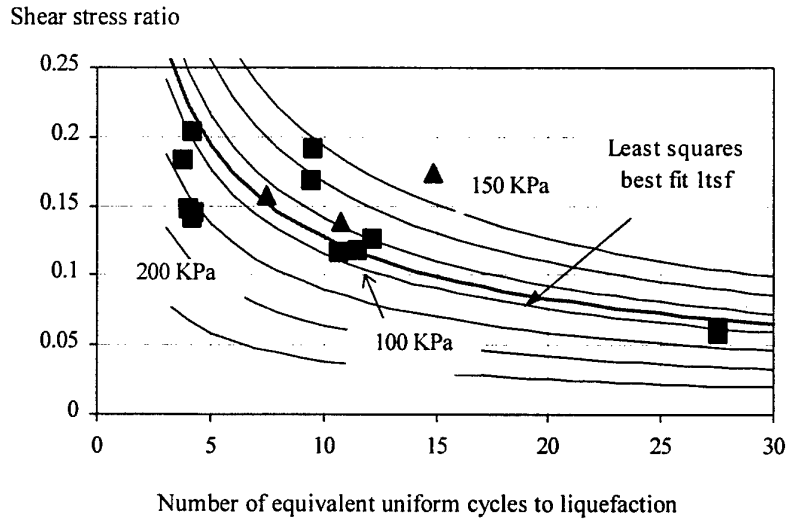


Figure 4.8 Comparison between first earthquake data and the shape of the liquefaction curves predicted using the MSFs by Idriss

Using the same family of curves, each data point was then scaled to its equivalent stress ratio at 10 cycles. As

$$(\tau/\sigma'_v)_N = (\tau/\sigma'_v)_{N=15} \cdot A N^{-B}$$

where A and B are the factors describing the family of curves, and therefore

$$(\tau/\sigma'_v)_{N=10} = (\tau/\sigma'_v)_{N=15} \cdot A 10^{-B}$$

then

$$(\tau/\sigma'_v)_{N=10} = (\tau/\sigma'_v)_N \cdot 10^{-B} / N^{-B}$$

4.6 Comparison between centrifuge $K\sigma$ and laboratory $K\sigma$ results

The ratio of the equivalent cyclic stress ratio at ten cycles (defined as the liquefaction cyclic resistance strength ratio CRR) to the cyclic stress ratio at 10 cycles for the best fit 1tsf curve was calculated, giving K_σ , as shown in Figure 4.9.

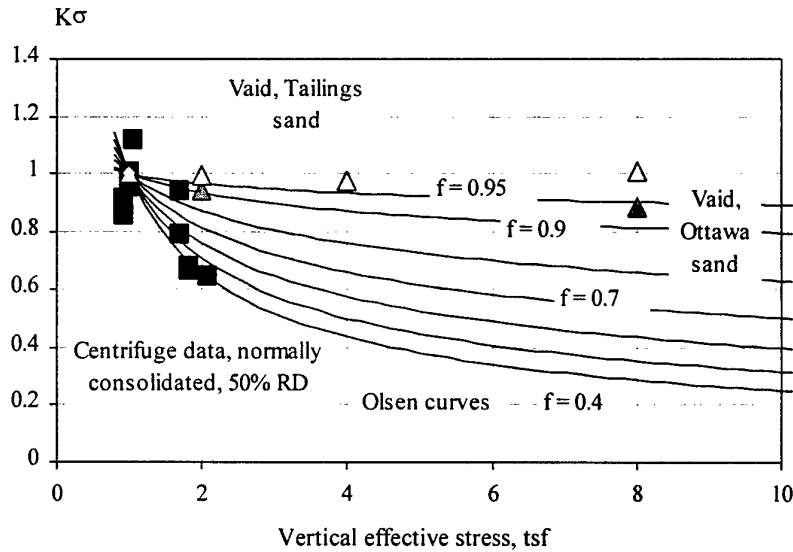


Figure 4.9 Comparison between first earthquake data (50% RD, normally consolidated only), expressed as $K\sigma$ at 10 cycles, compared with Olsen (1984) and laboratory test data from Vaid for Tailings and Ottawa sand

Figure 4.9 also includes data of $K\sigma$ calculated by Hynes and Olsen from laboratory test data of Vaid on Tailings sand and Ottawa sand. The curves shown in the figure were calculated using Olsen's function $K\sigma = (\sigma'_v)^{f-1}$, Olsen (1984).

Shear stress ratio

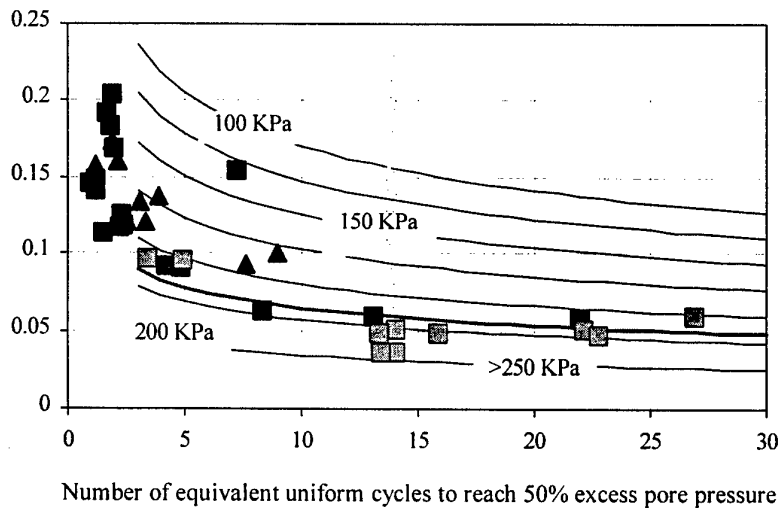
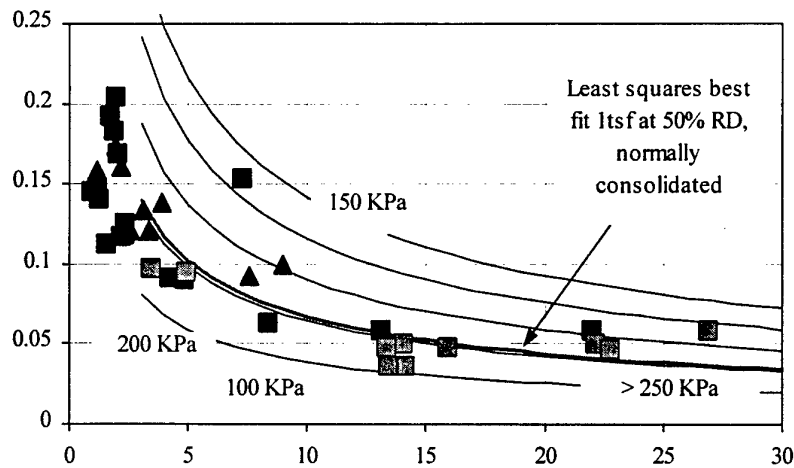


Figure 4.10 Comparison between all data and the shape of the liquefaction curves predicted using the MSFs of Seed & Idriss at 50% excess pore pressure, first earthquakes only

Shear stress ratio



Number of equivalent uniform cycles to reach 50% excess pore pressure

Figure 4.11 Comparison between all first earthquake data and the shape of the liquefaction curves predicted using the MSFs by Idriss at 50% excess pore pressure

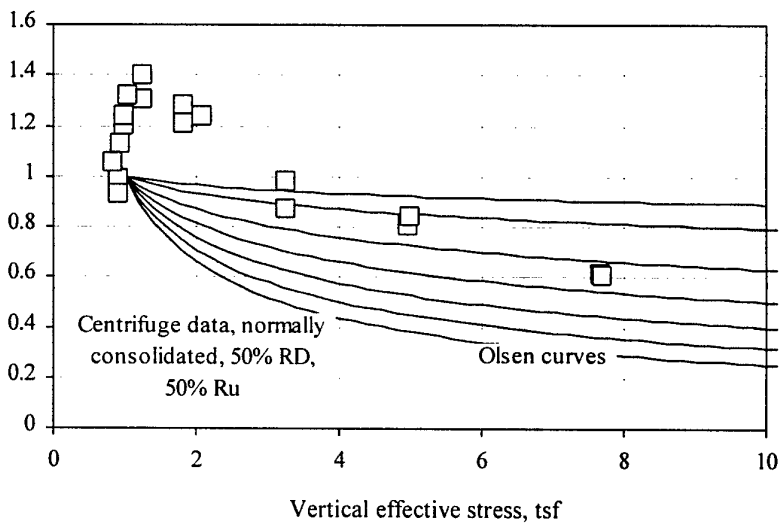
 $K\sigma$ 

Figure 4.12 Comparison between first earthquake data (50% RD, normally consolidated only) expressed as $K\sigma$ at 10 cycles for 50% excess pore pressure, compared with Olsen (1984), calculated using Seed MSFs

The range of data which showed 90% plus excess pore pressure generation was limited to relatively shallow depths. A second calculation was made to assess the value of $K\sigma$ at 50% excess pore pressure development. In this case, although the data are more constrained in terms of number of cycles to reach 50%, it is clear from Figures 4.10 and 11 that neither the Idriss MSF or the Seed and Idriss equivalent follow the trend of the data at both low and high numbers of cycles. This has a significant effect on the calculation of $K\sigma$, as shown in Figures 4.12 and 4.13.

$K\sigma$

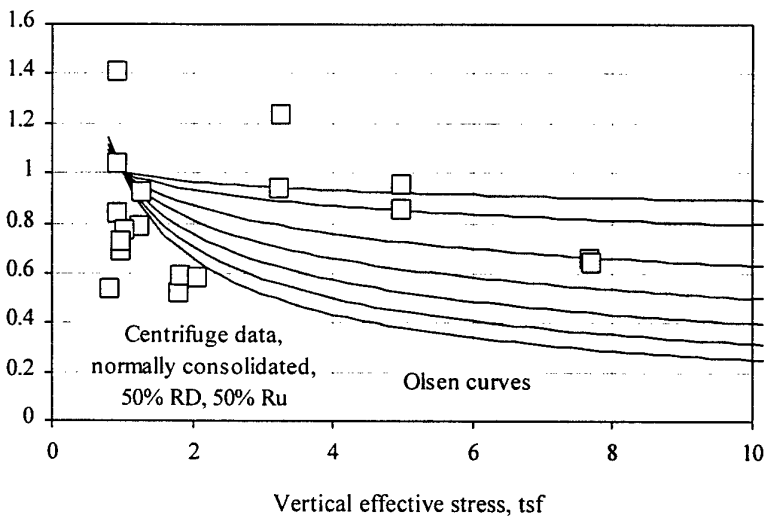


Figure 4.13 Comparison between first earthquake data (50% RD, normally consolidated only) expressed as $K\sigma$ at 10 cycles for 50% excess pore pressure, compared with Olsen (1984), calculated using Idriss MSFs

It is clear that the values of $K\sigma$ are highly sensitive to the selection of the shape of the characteristic curve, which is markedly flatter at high numbers of cycles than the standard MSFs would predict. The variability of $K\sigma$ is widely remarked upon in the literature, Youd and Idriss (1997).

4.7 Comparison with 'Stress focus' concept

Alternative representations of the CRR and CR as a function of depth have been proposed in order to support the extrapolation of K_s from low to high effective confining pressures. Hynes (1998) describe the use of log-log plots of CRR and CR vs depth to indicate the 'stress focus', towards which liquefaction resistance measured under low effective confining stress may be extrapolated to deduce resistance under high effective confining stress.

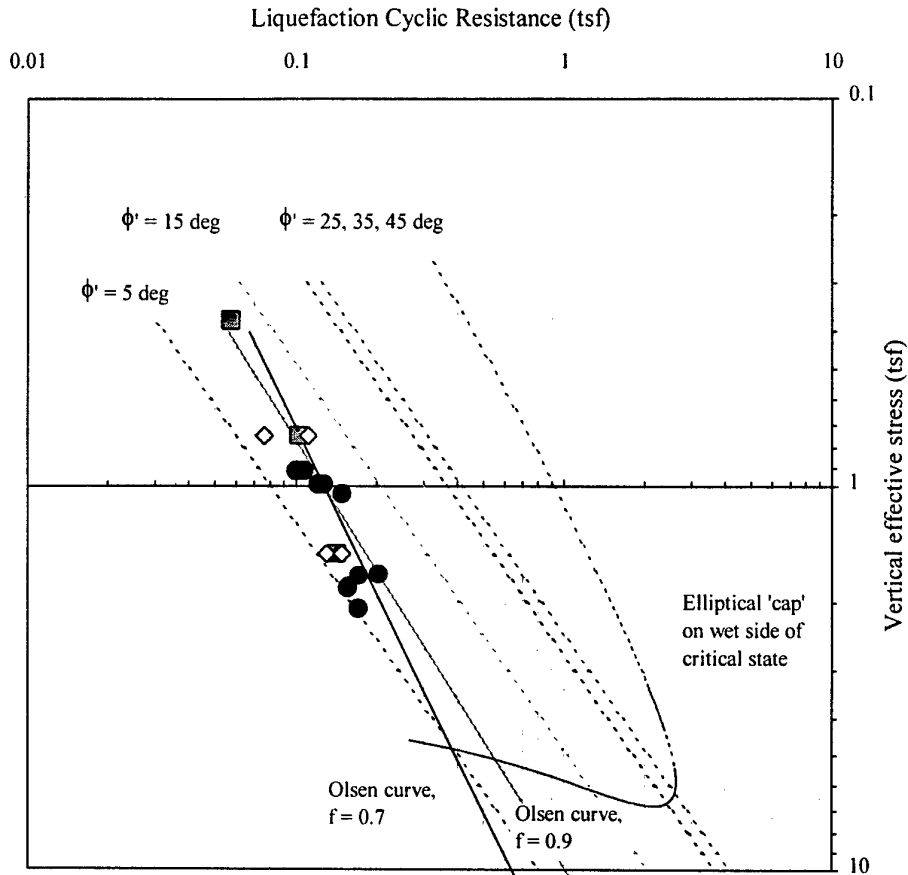


Figure 4.14 Stress focus plot using centrifuge data, normally consolidated, 50% RD, computed for 10 cycles using Idriss MSF, and compared with VELACS laboratory test data on Nevada sand corrected to 50% RD (CIUCyclic squares, CSS diamonds) and projected to 10 cycles using Seed MSF

The data from the centrifuge experiments are shown in log CRR - log depth form in Figure 4.14. Two curves, representing $f = 0.7$ and $f = 0.9$ were drawn through the CRR at 1 tsf. (For the centrifuge data, this was the best fit value. For Vaid's data, this was the 1 tsf value.) Also shown in the figure are laboratory test data carried out by Earth Technology Corporation for the VELACS project.

[The laboratory test data were processed as follows. Seven experiments were identified from the VELACS data, three undrained cyclic triaxial tests (CIUCyclic) and four undrained cyclic simple shear tests (CSS). These were conducted on sand at 60% RD. The triaxial data was converted to a simple shear equivalent using a factor of $2/\sqrt{3} \times q/2 / \sigma'_3$, following Castro. The data was then further adjusted for relative density using the Holtz and Gibbs relation for SPT and relative density for coarse sand. At 1 tsf, the number of blows at 50% RD is around 10. At 60%, this rises to around 13.4. From Seed for a Magnitude 7.5 earthquake the CSR at 50% is around 0.102 and at 60% is around 0.14. hence the data is scaled by a factor of 0.729. Finally, the data was extrapolated to the equivalent CSR at 10 cycles. This was done using both the Idriss curve and the flatter Seed curve. It was found that the flatter Seed curves collapsed the laboratory data on top of the centrifuge data much more closely than the Idriss curve (which more closely reflected the centrifuge data). These

laboratory test data for Nevada sand were then plotted in Figure 4.15, using solid squares for the triaxial data and open diamonds for the simple shear data.]

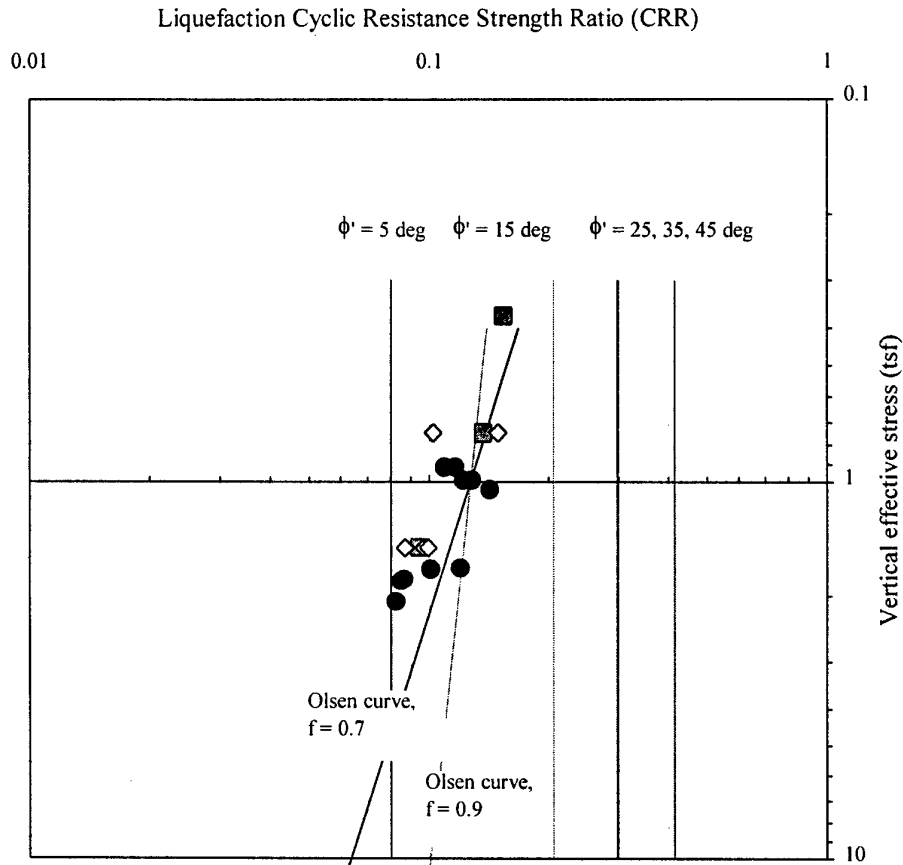


Figure 4.15 Stress focus plot using centrifuge data, normally consolidated, 50% RD, computed using Idriss MSF for 10 cycles, and compared with VELACS laboratory test data on Nevada sand corrected to 50% RD (CIUCyclic squares, CSS diamonds) and projected to 10 cycles using Seed MSF

Figure 4.15 shows the comparable plot of CR as a function of depth. Recalling that the CRR and CR are calculated essentially by dividing the applied cyclic shear stress at initial liquefaction by the initial effective confining stress (and scaling to ten cycles), it is instructive to compare the data with 'true' stress ratios denoted as mobilised angles of shearing resistance ϕ' in the conventional manner. These may be simply added as straight lines in both figures.

4.8 Stress path analysis

A full derivation of the stress path analysis is presented in Appendix B. The stress path for a typical soil element is shown in Figure 4.16, for Model 3c, earthquake 1, depth 22m (Table 3.2). The value of K_0 based on $K_0 = 1 - \sin \phi'$, where $\phi' = 33$ degrees as the boundary conditions for a soil element in the centrifuge specimen are the equivalent of zero lateral strain. Separate plots show the mean effective confining

stress, s' , the shear stress t and applied cyclic shear stress τ_{av} , and the 'true' mobilised angle of shearing resistance. The angle of shearing resistance computed for this data point based on the liquefaction cyclic resistance ratio, with $CRR = 0.0868$, $CR = 0.157$, $\sigma_{v0}' = 194 \text{ KPa}$ (1.81 tsf), is given by $\sin \phi' = CRR/(1-CRR)$, or $\phi' = 5.45$ degrees.

This data point reached the origin and a near zero effective stress state. However others, at higher effective confining stress, were observed not to reach the same state and despite continued cycling, the generation of excess pore pressure was limited. One such data-point was Model 4d, earthquake 2, shown in Figure 4.17. Here the stress path moves progressively towards the origin, excess pore pressure developing at a steady rate. After a number of cycles, excess pore pressure stops rising and the downward migration of the stress path is arrested. This point reached around 44% of the initial vertical effective stress.

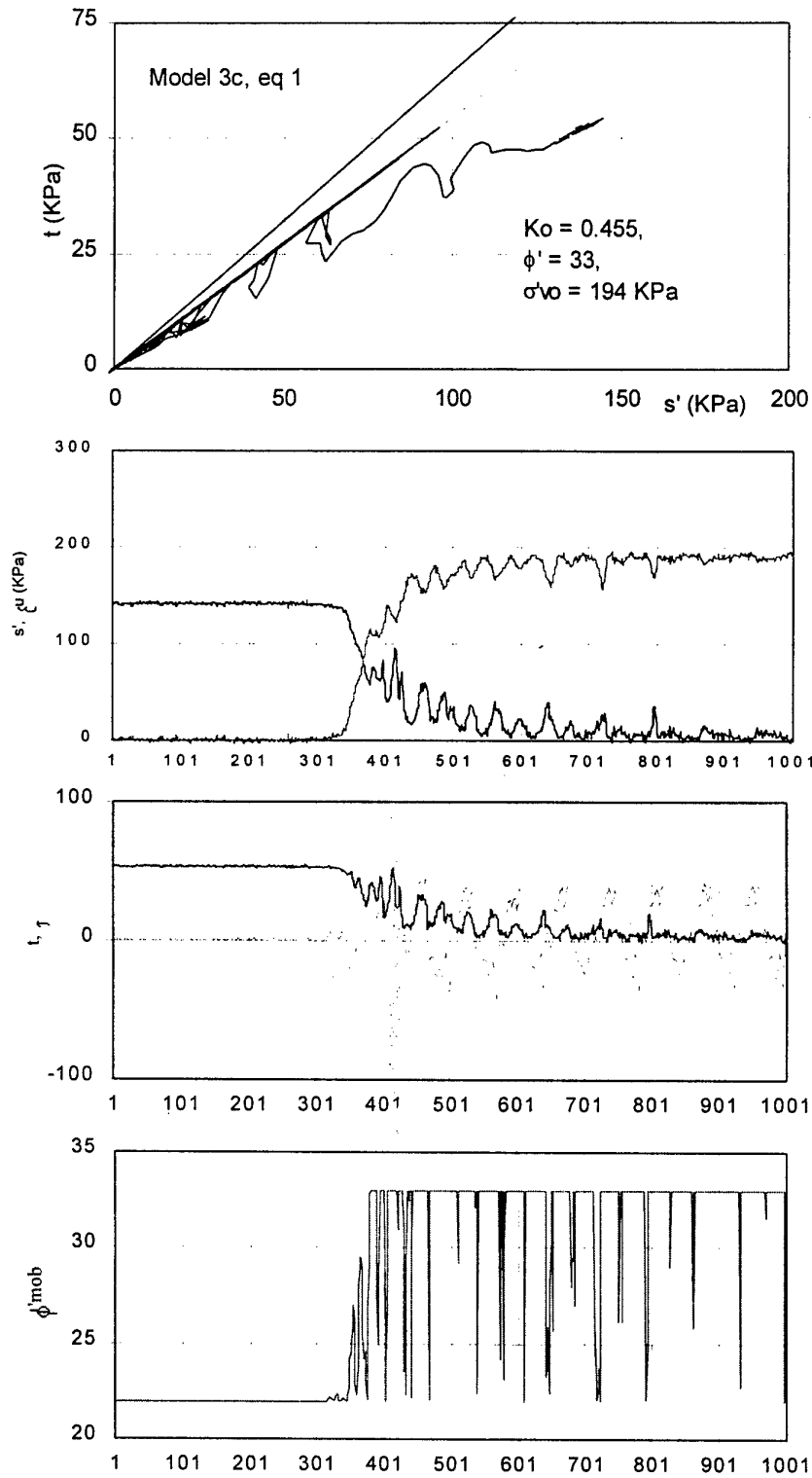


Figure 4.16 Stress path for soil element at initial vertical effective stress of 194 KPa

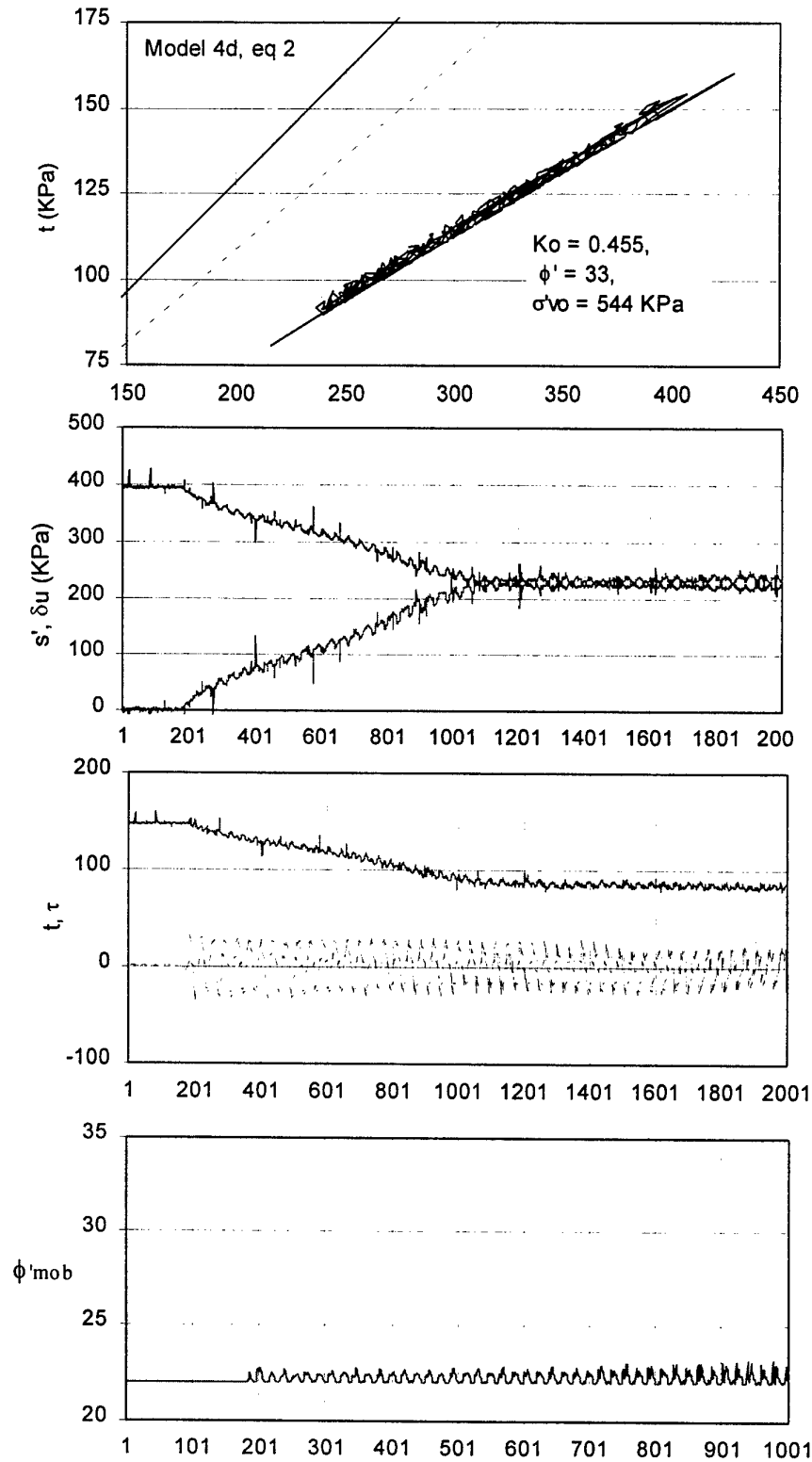


Figure 4.17 Stress path for soil element at initial vertical effective stress of 544 KPa

4.9 Data of excess pore pressures

Under high effective confining stresses, it was noted that in many cases, excess pore pressures did not reach the initial vertical effective stress, as was the case with data from shallow depths. Plotting all data points in Figure 4.18, it is clear that there is a reducing trend at initial vertical effective stresses above around 300 KPa and excess pore pressures do not reach sufficient levels to cause initial liquefaction, despite continued cycling. In this figure, data points include data of all densities, first and following earthquakes, normally and overconsolidated specimens.

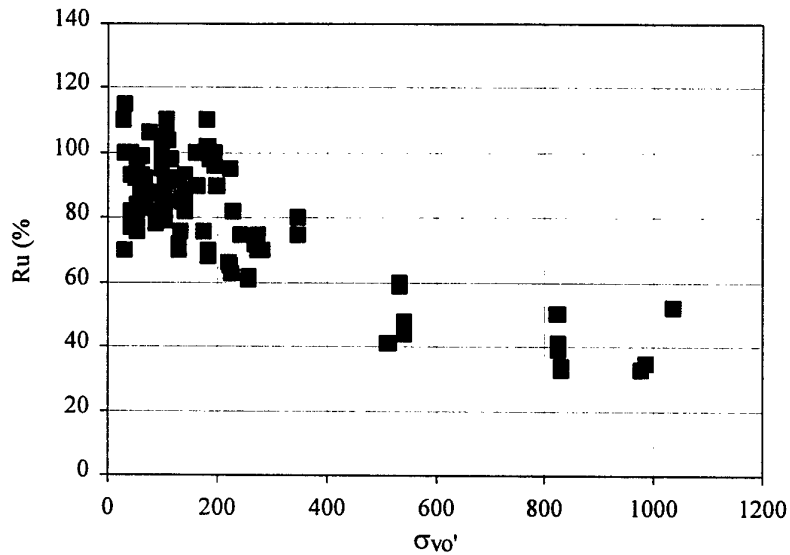


Figure 4.18 Comparison between upper limit of excess pore pressure generation and initial effective vertical stress, all data

A similar phenomenon has been observed in torsional simple shear tests, Ishihara (1996) from Ishihara and Nagase (1988). Fig. 19 shows that although there is a minor effect of overconsolidation, which appears to reduce the magnitude of the excess pore pressure slightly below that of the normally consolidated data, as might be expected. The trend with increasing effective vertical stress is identical, however.

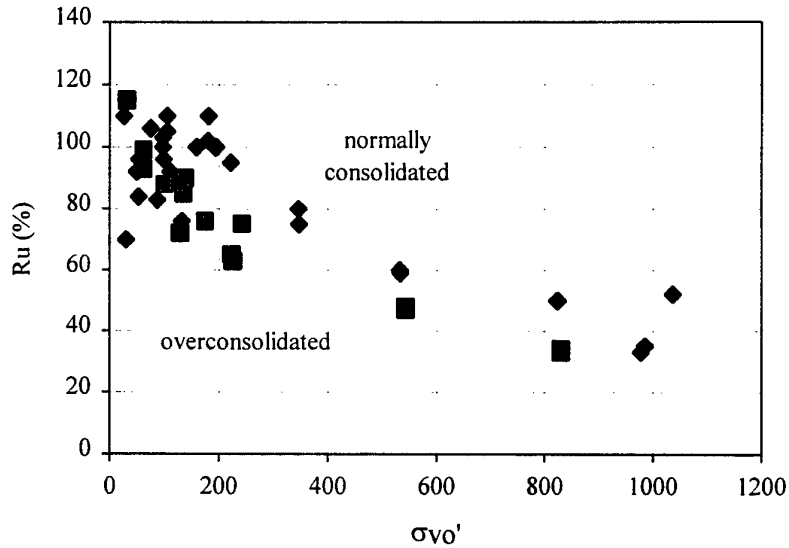


Figure 4.19 Comparison between upper limit of excess pore pressure generation and initial effective vertical stress, first earthquake data, normally and overconsolidated

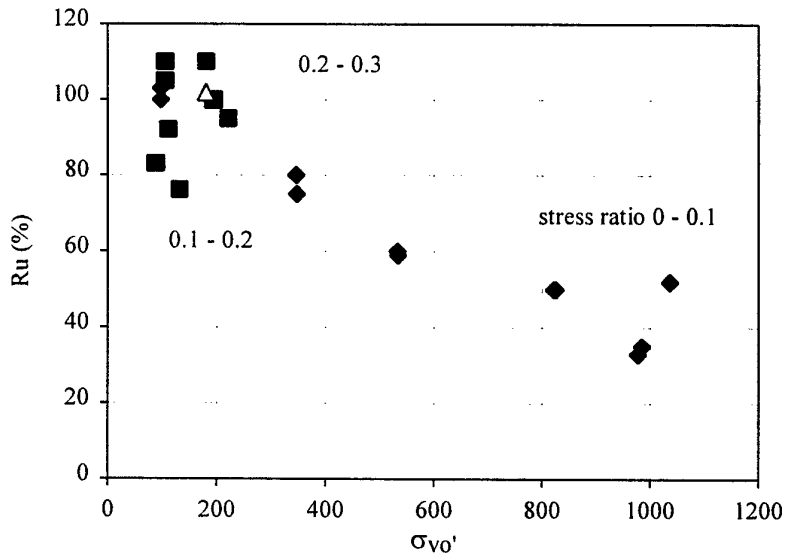


Figure 4.20 R_u as a function of stress ratio, for first earthquake <50% RD, normally consolidated data

Figure 4.20 shows a selection of the data, concentrating only on normally consolidated data from first earthquakes at 50% Relative Density or less. At an initial vertical effective stress of less than around 300 KPa, even low applied cyclic stress ratios are sufficient to achieve excess pore pressures of 100%. At higher vertical effective stresses, however, this is not the case and R_u falls progressively. Although most of the data is around 50% RD, the very highest effective confining stresses are associated with a low relative density (39%), which may explain the higher values of R_u than suggested by the general trend.

This phenomenon is not predicted using standard design methods.

Fig. 4.21 breaks the data out by earthquake, from which it is clear that there is little to distinguish between first and succeeding shaking events. The implication of this is that the pattern of excess pore pressure generation is very similar in successive earthquakes, showing the same limit and trend with depth.

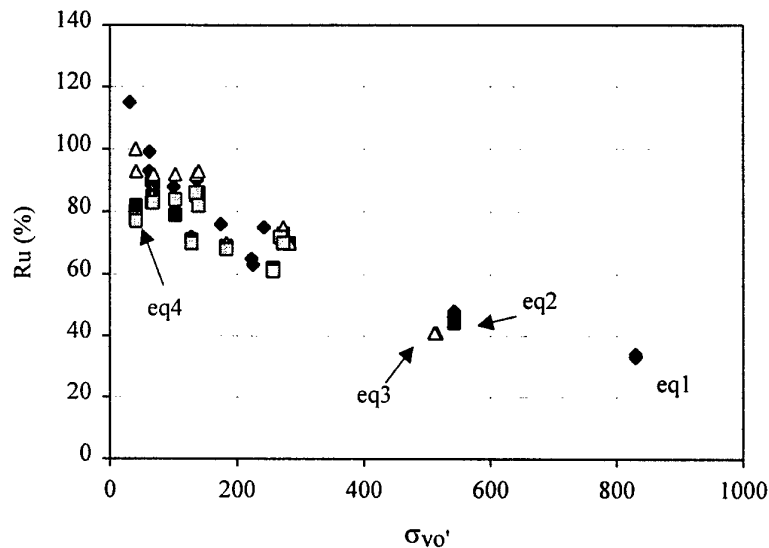


Figure 4.21 Comparison between upper limit of excess pore pressure generation and initial effective vertical stress, overconsolidated, by earthquake

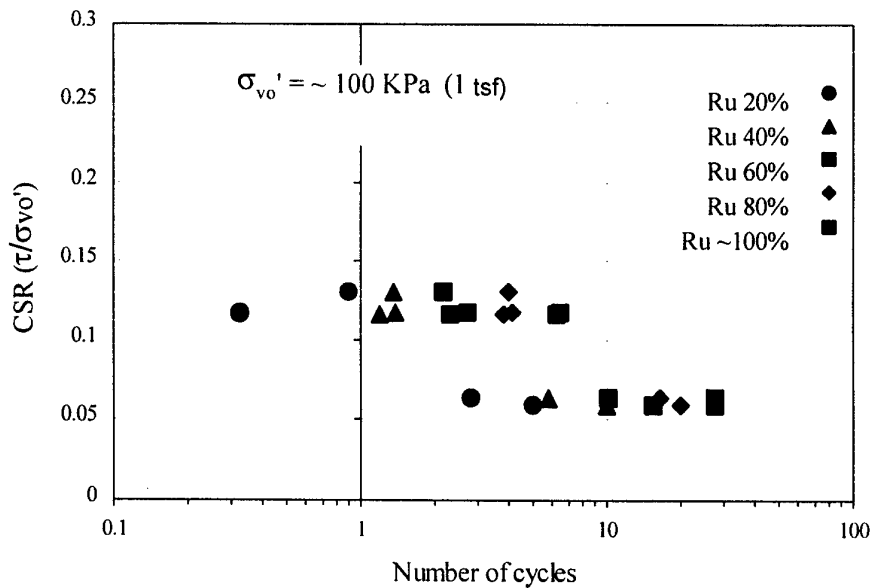


Figure 4.22 CSR as function of cycles and Ru (%), first earthquakes, <50% RD, normally consolidated data, 100 KPa (~1 tsf)

Finally, the relationship between stress ratio and number of cycles to reach different levels of excess pore pressure, expressed as R_u (%) is shown in Fig. 4.22. The curves appear to be broadly parallel to each other, rather than tending to merge at low values of CSR as would be predicted from laboratory element tests. This confirms that the observation of limited R_u with depth is not simply a consequence of low CSR.

5 CONCLUSIONS

1. A large database of the development of excess pore pressure in a uniform saturated sand bed has been established.
2. The extrapolation of the simplified procedure for the evaluation of liquefaction resistance using the correction factor $K\sigma$ may not be warranted at high confining stresses. The centrifuge derived values of $K\sigma$ do not match the laboratory developed values. This is probably because the laboratory cyclic triaxial test does not provide similar boundary conditions to the centrifuge model, which are considered to be more representative of the field conditions.
3. Observation of the stress path followed by soil elements as they approach a condition of near zero effective stress shows that the strength of the soil is not related to the initial effective vertical stress.
4. There is a cut-off in the development of excess pore pressure which is a function of the initial vertical effective stress. Further studies are required to confirm that this cap is likely also to be a function of earthquake amplitude and is probably associated with strain amplitude.
5. It is postulated that the relationship between R_u and shear strain derived from laboratory element test data may be conservative when applied to centrifuge or field boundary conditions.
6. The implications of this finding are significant for the assessment of the risk posed by earthquakes to large earth dams and similar structures, where the high effective confining stresses in the foundations may lead to an overly conservative assessment of the requirement for remediation.

6 REFERENCES

- Byrne, P. M. And Harder, L. F., (1991). Terzaghi Dam, Review of Deficiency Investigation, Report No. 3, prepared for B C Hydro, Vancouver, British Columbia.
- Butler, G.D., (1998). A Dynamic Analysis Of The Stored Angular Momentum Actuator Used With The Equivalent Shear Beam Container, Ph.D. thesis, University of Cambridge, England.
- Finn, W. D. Liam and Ledbetter, R. H., (1991). Evaluation of Liquefaction Effects and Remediation Strategies by Deformation Analysis, *Proceedings, International Conference on Geotechnical Engineering for Coastal Development, GEOCOAST 91*, Yokohama, Japan.
- Finn, W. D. Liam, Ledbetter, R. H., Fleming, R. L., Jr., Templeton, A. E., Forrest, T. W., and Stacy, S. T., (1991). Dam on Liquefiable Foundation: Safety Assessment and Remediation, *17th Congress on Large Dams, International Commission on Large Dams*, Vienna, Austria.
- Finn, W. D. Liam, Ledbetter, R. H., and Marcuson, W. F., III, (1994). Seismic Deformations in Embankments and Slopes, *Proceedings, Symposium on Developments in Geotechnical Engineering (From Harvard to New Delhi, 1936 - 1994)*, Bangkok, Thailand.
- Hynes, M. E. (1998). Influence of confining stress on liquefaction resistance, Proc Int Workshop on the Physics and Mechanics of Soil Liquefaction, Baltimore, MD, 10-11 Sept, A A Balkema.
- Ledbetter, R. H., (1991). Large Centrifuge: A Critical Army Capability For The Future, Miscellaneous Paper GL-91-12, U.S. Army Engineer Waterways Experiment Station, Vicksburg, MS.
- Ledbetter, R. H. and Finn, W. D. Liam, (1993). Development and Evaluation of Remediation Strategies by Deformation Analysis, *Proceedings of the specialty conference Geotechnical Practice in Dam Rehabilitation*, Raleigh, North Carolina, Geotechnical Special Publication No. 35.
- Ledbetter, R. H., Finn, W. D. Liam, Hynes, M. E., Nickell, J. S., Allen, M. G., and Stevens, M. G., (1994). Seismic Safety Improvement of Mormon Island Auxiliary Dam, *18th Congress on Large Dams, International Commission on Large Dams*, Durban, South Africa.
- Madhabushi, S. P. G., (1996). Preliminary Centrifuge Tests Using The Stored Angular Momentum (SAM) Earthquake Actuator, Cambridge University Engineering Department report, Cambridge University, England.
- National Center for Earthquake Engineering Research (NCEER), (1996). Workshop on Evaluation of Liquefaction Resistance, Salt Lake City, Utah.

- Newmark, N. M., (1965). Effects of Earthquakes on Dams and Embankments, *5th Rankine Lecture, Geotechnique*, Vol. 15, No. 2.
- Olsen, R. S., (1994). Normalisation and prediction of geotechnical properties using the Cone Penetrometer Test (CPT), PhD Thesis, University of California, Berkeley.
- Olsen, R. S., (1996). The Influence of Confining Stress on Liquefaction Resistance, *Draft WES Report*.
- Peck, R. B., (1992). Written comments on the review of remediation for Mormon Island Auxiliary Dam.
- Pillai, V. S. and Byrne, P. M., (1994). Effect of Overburden Pressure on Liquefaction Resistance of Sand, *Canadian Geotechnical Journal*, Vol. 31.
- Schofield, A. N., (1981). Dynamic and Earthquake Geotechnical Centrifuge Modelling, *Proceedings, International Conference on Recent Advances in Geotechnical Earthquake Engineering and Soil Dynamics*, University Missouri Rolla, MO, Vol. 3.
- Schofield, A. N. and Steedman, R. S., (1988). Recent Development of Dynamic Model Testing in Geotechnical Engineering, *Proceedings, 7th World Conference in Earthquake Engineering*, Tokyo-Kyoto, Vol. VIII.
- Seed, H. B., (1979). Considerations in the Earthquake-Resistant Design of Earth and Rockfill Dams, *19th Rankine Lecture, Geotechnique*, Vol. 29, No. 3.
- Seed, R. B. and Harder, L. F., (1990). SPT-Based Analysis of Cyclic Pore Pressure Generation and Undrained Residual Strength, *Proceedings of the H. Bolton Seed Memorial Symposium*, University of California, Berkeley, Vol. 2.
- Steedman, R.S. (1999) Earthquake Engineering Support, Phase 2 Final Technical Report, N68171-98-C-9014, European Office of the U.S. Army, London, January.
- Vaid, Y. P. and Chern, J. C., (1985). Cyclic and Monotonic Undrained Response of Saturated Sands, *Advances in the Art of Testing Soils under Cyclic Conditions, ASCE Convention*, Detroit.
- Vaid, Y. P. and Thomas, J., (1994). Post Liquefaction Behavior of Sand, *Proceedings of the 13th International Conference on Soil Mechanics and Foundation Engineering*, New Delhi, India.
- Zeng, X. and Schofield, A. N., (1996). Design and Performance of an Equivalent-Shear-Beam Container for Earthquake Centrifuge Modelling, *Geotechnique*, Vol. 46, No. 1.

APPENDIX A

Dataset of all models

EQEN Earthquake model test data

Last update: 30 June 1999

By: RSS

Data of limiting pore pressures, Models and cycles

| Model, Earthquake | Eq | Centrifg acc'n | Total vertical stress (kPa) | Effective Pressure (kPa) | Cycles to upper limit | Cycles to 50% excess | Pore pressure Upper limit (%) | Upper value (kPa) | Actual stress ratio | Stress ratio | Relative Density (%) | Quality low/med/high/* | Comments PPT |
|----------------------|----|-------------------|--------------------------------------|--------------------------------|-----------------------------|----------------------------|--|-------------------------|---------------------------|-----------------|----------------------------|---------------------------|---|
| Model 1a, 1 | 1 | 50 | 67.6 | 34 | 10.8 | | 59 | 20.06 | 0.105 | 0.068 | 70 | low | 31 Uncertain measured depth of transducers, showed double frequency |
| Model 1a, 1 | 1 | | | | | | | | | | | | 10 Still climbing at end of datacapture |
| Model 1a, 1 | 1 | | | | | | | | | | | | 9 Still climbing at end of datacapture |
| Model 1a, 2 | 2 | 50 | 67.6 | 35 | 12.4 | | 100 | 35 | | 0.0511 | 70 | low | 31 Ottawa sand. Second eq showed slow rise to final limit |
| Model 1a, 2 | 2 | | | | | | | | | | | | 10 Still climbing at end of datacapture |
| Model 1a, 2 | 2 | | | | | | | | | | | | 9 Still climbing at end of datacapture |
| Model 2a, 1 | 1 | 50 | 70.3 | 30 | 2.51 | | 100 | 30 | 0.318 | 0.207 | 83 | low | Near surface acceleration clearly shows liquefaction |
| Model 2a, 2 | 2 | 50 | 70.3 | 30 | 2.48 | | 100 | 30 | 0.25 | 0.162 | 83 | low | Estimated as no ppts functioning |
| Model 2a, 3 | 3 | | | | | | | | | | | | Probably did not liquefy |
| Model 2b, 1 | 1 | 50 | 221 | 106 | 10.719 | 2.187 | 110 | 116.6 | 0.18 | 0.117 | 50 | * | 10 Clearly over 100%, large cycles affect 50% point |
| Model 2b, 1 | 1 | 50 | 223 | 106 | 11.529 | 2.349 | 105 | 111.3 | 0.181 | 0.118 | 50 | * | 30 Double frequency just over 100%, large cycles affect 50% point |
| Model 2b, 1 | 1 | 50 | 68.9 | 27 | 10.611 | 2.16 | 110 | 29.7 | 0.292 | 0.19 | 75 | * | 31 Clearly over 100%, large cycles affect 50% point |
| Model 2b, 2 | 2 | 50 | 230 | 111 | 5.4 | | 104 | 115.44 | 0.221 | 0.143 | 50 | * | 10 Very clearly 100% |
| Model 2b, 2 | 2 | 50 | 236 | 115 | 4.59 | | 98 | 112.7 | 0.216 | 0.141 | 50 | * | 30 Rapid rise to 100% |
| Model 2b, 2 | 2 | 50 | 76.4 | 32 | 5.4 | | 100 | 32 | 0.33 | 0.214 | 75 | * | 31 Clear 100%, rapid rise |
| Model 2c, 1 | 1 | 50 | 240 | 98 | 27.5 | 13.095 | 100 | 98 | 0.092 | 0.059 | 49 | high | 46 Possibly just reached limit before being cut off |
| Model 2c, 1 | 1 | 50 | 256 | 98 | 27.5 | 8.343 | 103 | 100.94 | 0.097 | 0.063 | 49 | high | 41 Seems to be very close to limit at the end of the eq |
| Model 2c, 1 | 1 | 50 | | 99 | | 21.978 | | | 0.0899 | 0.0585 | 49 | high | 49 Still climbing when data cut off |
| Model 2c, 1 | 1 | 50 | 69.2 | 30 | 8.59 | 5.238 | 70 | 21 | 0.114 | 0.074 | 74 | high | 37 Reached upper limit early, unlike other depths, high freq rapid rise affects 50% point |
| Model 2c, 1 | 1 | | | | | | | | | | | | 42 Erratic response, still climbing at end |
| Model 2c, 1 | 1 | | | | | | | | | | | | 39 Erratic response, still climbing at end |

| | | | | | | | | | | | |
|-------------|---|----|------|------|------|-------|--------|--------|-------|---------|---|
| Model 2c, 2 | 2 | 50 | 240 | 98 | 46 | 96 | 94.08 | 0.094 | 0.061 | 49 high | 46 Very close to limit at end |
| Model 2c, 2 | 2 | 50 | 256 | 98 | 46 | 100 | 98 | 0.1 | 0.065 | 49 high | 41 Very close to limit at end |
| Model 2c, 2 | 2 | | | | | | | | | | 49 Still climbing at end of shaking |
| Model 2c, 2 | 2 | 50 | 70.8 | 27.6 | 6.6 | 75 | 20.7 | 0.132 | 0.085 | 74 med | 37 Reached upper limit early, unlike other depths |
| Model 2c, 2 | 2 | | | | | | | | | | 42 Erratic response, still climbing at end |
| Model 2c, 2 | 2 | 50 | 74.1 | 30.3 | 12.8 | 90 | 27.27 | 0.123 | 0.08 | 74 med | 39 Reached upper limit early, like ppt37 |
| Model 2c, 3 | 3 | | | | | | | | | | 46 Still climbing at end of shaking |
| Model 2c, 3 | 3 | | | | | | | | | | 41 Still climbing at end of shaking |
| Model 2c, 3 | 3 | | | | | | | | | | 49 Still climbing at end of shaking |
| Model 2c, 3 | 3 | 50 | 70.8 | 27.6 | 7.7 | 70 | 19.32 | 0.127 | 0.083 | 74 med | 37 Reached upper limit early, very noisy response |
| Model 2c, 3 | 3 | | | | | | | | | | 42 Erratic response, still climbing at end |
| Model 2c, 3 | 3 | 50 | 74.1 | 30.3 | 15.4 | 80 | 24.24 | 0.069 | 0.045 | 74 med | 39 Reached upper limit later than ppt37, very noisy |
| Model 2c, 4 | 4 | | | | | | | | | | 46 Still climbing at end of shaking |
| Model 2c, 4 | 4 | | | | | | | | | | 41 Still climbing at end of shaking |
| Model 2c, 4 | 4 | | | | | | | | | | 49 Still climbing at end of shaking |
| Model 2c, 4 | 4 | 50 | 70.8 | 27.6 | 5.4 | 70 | 19.32 | 0.107 | 0.07 | 74 med | 37 Reached upper limit early, very noisy response |
| Model 2c, 4 | 4 | | | | | | | | | | 42 Erratic response, still climbing at end |
| Model 2c, 4 | 4 | 50 | 74.1 | 30.3 | 36.5 | 75 | 22.725 | 0.1 | 0.065 | 74 med | 39 Possibly reached limit, very noisy |
| Model 2c, 5 | 5 | | | | | | | | | | 46 No excess pore pressure |
| Model 2c, 5 | 5 | | | | | | | | | | 41 No excess pore pressure |
| Model 2c, 5 | 5 | | | | | | | | | | 49 No excess pore pressure |
| Model 2c, 5 | 5 | | | | | | | | | | 37 No excess pore pressure |
| Model 2c, 5 | 5 | | | | | | | | | | 42 No excess pore pressure |
| Model 2c, 5 | 5 | | | | | | | | | | 39 No excess pore pressure |
| Model 2d, 1 | 1 | 50 | 188 | 76 | 9.45 | 1.998 | 80.56 | 0.26 | 0.169 | 74 * | 3 Good record, dense/loose boundary |
| Model 2d, 1 | 1 | 50 | 203 | 88 | 5 | 1.539 | 83 | 73.04 | 0.174 | 49 * | 31 Double frequency at upper limit suggests 100% excess pwp |
| Model 2d, 1 | 1 | 50 | 317 | 133 | 13 | 2.565 | 76 | 101.08 | 0.187 | 49 high | 46 Difficult to identify upper limit, which rises slowly, large cycles affect 50% point |
| Model 2d, 1 | 1 | 50 | 124 | 50 | 10 | 2.322 | 92 | 46 | 0.25 | 74 high | 7 Sank during earthquake, clearly reached limit |
| Model 2d, 1 | 1 | 50 | 150 | 59.4 | 8.4 | 1.755 | 93 | 55.242 | 0.242 | 74 * | 41 Clearly reached limit, dense/loose boundary, large cycles affect 50% point |
| Model 2d, 1 | 1 | 50 | 264 | 112 | 12.2 | 2.322 | 92 | 103.04 | 0.193 | 49 high | 51 Reached limit, cyclic response, large cycles affect 50% point |
| Model 2d, 1 | 1 | 50 | | 135 | | 3.348 | | | 0.186 | 49 high | 8 Still climbing slowly at end of shaking, large cycles affect 50% point |
| Model 2d, 2 | 2 | 50 | 195 | 76 | 9.2 | | 88 | 66.88 | 0.338 | 74 * | 3 Good record, dense/loose boundary |
| Model 2d, 2 | 2 | 50 | 204 | 86.6 | 4 | | 80 | 69.28 | 0.299 | 49 * | 31 Double frequency at upper limit suggests 100% excess pwp |

| | | | | | | | | | | | | |
|-------------|---|-----|------|-------|-------|-----|--------|-------|-------|---------|----|---|
| Model 2e, 4 | 4 | 125 | 381 | 184 | 11.1 | 68 | 125.12 | 0.149 | 0.097 | 49 high | 49 | Very rapid immediate response, then slow rise to limit, as above |
| Model 2e, 4 | 4 | 125 | 68.9 | 42.4 | 7.1 | 67 | 28.408 | 0.166 | 0.108 | 73 med | 43 | Dense layer, reached some sort of limit but noisy signal |
| Model 2f, 1 | 1 | 125 | 172 | 63 | 15.4 | 99 | 62.37 | 0.288 | 0.187 | 50 * | 31 | Excellent, loose/dense interface |
| Model 2f, 1 | 1 | 125 | 251 | 101 | 13.5 | 88 | 88.88 | 0.237 | 0.154 | 50 * | 47 | Excellent, up to 7.911 for 50% |
| Model 2f, 1 | 1 | 125 | 320 | 136 | 7.34 | 85 | 115.6 | 0.207 | 0.134 | 50 * | 46 | Excellent |
| Model 2f, 1 | 1 | 125 | 104 | 32.2 | 5.21 | 115 | 37.03 | 0.395 | 0.257 | 75 * | 38 | Excellent |
| Model 2f, 1 | 1 | 125 | 102 | 31.7 | 5.4 | 115 | 36.455 | 0.397 | 0.258 | 75 * | 51 | Clear limit, very rapid rise with one or two big cycles, affecting 50% |
| Model 2f, 1 | 1 | 125 | 172 | 62.6 | 13.5 | 93 | 58.218 | 0.293 | 0.191 | 50 * | 15 | Good record, loose/dense interface |
| Model 2f, 1 | 1 | 125 | 337 | 138 | 10.8 | 90 | 124.2 | 0.213 | 0.138 | 50 * | 41 | Bottom of loose layer, rapid rise to limit, with cycles which may affect 50% |
| Model 2f, 2 | 2 | 125 | 177 | 69 | 8.6 | 88 | 60.72 | 0.287 | 0.187 | 50 * | 31 | Excellent |
| Model 2f, 2 | 2 | 125 | 254 | 103.5 | 14 | 79 | 81.765 | 0.248 | 0.161 | 50 * | 47 | Good record |
| Model 2f, 2 | 2 | 125 | 320 | 136 | 2.2 | 85 | 115.6 | 0.222 | 0.144 | 50 * | 46 | Very rapid rise to limit |
| Model 2f, 2 | 2 | 125 | 113 | 41.4 | 3.2 | 80 | 33.12 | 0.341 | 0.222 | 75 * | 38 | Clear limit, slightly noisy |
| Model 2f, 2 | 2 | 125 | 112 | 41.9 | 4.1 | 82 | 34.358 | 0.336 | 0.218 | 75 * | 51 | Clear limit, again noisy |
| Model 2f, 2 | 2 | 125 | 177 | 67.6 | 20.3 | 85 | 57.46 | 0.294 | 0.191 | 50 * | 15 | Two stage rise to final limit |
| Model 2f, 2 | 2 | 125 | 339 | 140.3 | 6.8 | 86 | 120.65 | 0.225 | 0.146 | 50 * | 41 | Bottom of model, rapid rise to limit |
| Model 2f, 3 | 3 | 125 | 177 | 69 | 19.7 | 92 | 63.48 | 0.38 | 0.247 | 50 high | 31 | Reached limit near end of shaking, loose/dense interface |
| Model 2f, 3 | 3 | 125 | 254 | 103.5 | 34.8 | 92 | 95.22 | 0.328 | 0.213 | 50 high | 47 | Just reached limit near end |
| Model 2f, 3 | 3 | 125 | 320 | 136 | 4.3 | 92 | 125.12 | 0.293 | 0.191 | 50 * | 46 | Bottom of model, very rapid rise to limit |
| Model 2f, 3 | 3 | 125 | 113 | 41.4 | 6.2 | 100 | 41.4 | 0.452 | 0.293 | 75 * | 38 | Clear limit, slightly noisy |
| Model 2f, 3 | 3 | 125 | 112 | 41.9 | 4.9 | 93 | 38.967 | 0.444 | 0.288 | 75 * | 51 | Clear limit, again noisy |
| Model 2f, 3 | 3 | 125 | 339 | 140 | 10.3 | 93 | 130.2 | 0.298 | 0.193 | 50 * | 15 | Still rising at end of shaking |
| Model 2f, 3 | 3 | 125 | 177 | 69 | 26.2 | 83 | 57.27 | 0.39 | 0.254 | 50 high | 41 | Bottom of model, rapid rise to limit |
| Model 2f, 4 | 4 | 125 | 254 | 103.5 | 23.5 | 84 | 86.94 | 0.337 | 0.219 | 50 high | 31 | Reached limit near end of shaking, cyclic response |
| Model 2f, 4 | 4 | 125 | 320 | 135.7 | 4.6 | 86 | 116.70 | 0.301 | 0.196 | 50 * | 47 | Reached limit near end |
| Model 2f, 4 | 4 | 125 | 113 | 41.4 | 7.3 | 78 | 32.292 | 0.463 | 0.301 | 75 * | 46 | Bottom of model, very rapid rise to limit |
| Model 2f, 4 | 4 | 125 | 112 | 41.9 | 4.6 | 77 | 32.263 | 0.455 | 0.296 | 75 * | 38 | Clear limit, slightly noisy |
| Model 2f, 4 | 4 | 125 | 339 | 140.3 | 15.4 | 82 | 115.04 | 0.305 | 0.199 | 50 * | 51 | Clear limit, again noisy |
| Model 2f, 4 | 4 | 125 | 474 | 181 | 4.185 | 102 | 184.62 | 0.314 | 0.204 | 34 high | 15 | Still rising at end of shaking |
| Model 2f, 4 | 4 | 125 | 429 | 182 | 3.78 | 110 | 200.2 | 0.281 | 0.183 | 34 high | 41 | Bottom of model, slower rise to limit |
| Model 3a, 1 | 1 | 50 | 474 | 181 | 4.185 | 102 | 184.62 | 0.314 | 0.204 | 34 high | 9 | Spiky acceleration record, but excellent pore pressure data, rapid rise affects 50% |
| Model 3a, 1 | 1 | 50 | 429 | 182 | 3.78 | 110 | 200.2 | 0.281 | 0.183 | 34 high | 10 | Low static pore pressure value, good dynamic response. |

| | | | | | | | | | | | | |
|-------------|---|---|----|-----|------|-------|-----|--------|-------|-------|---------|---|
| Model 3a, 2 | 2 | 2 | 50 | 477 | 186 | 7.911 | 98 | 182.28 | 0.288 | 0.187 | 34 high | rapid rise affects 50% |
| Model 3a, 2 | 2 | 2 | 50 | 432 | 184 | 3.591 | 102 | 187.68 | 0.258 | 0.168 | 34 high | 9 Slow rise contrasts with ppt10 |
| Model 3b, 2 | 2 | 2 | 50 | 466 | 198 | 5.427 | 90 | 178.2 | 0.124 | 0.081 | 49 med | 10 Good limit, spikier acceleration on eqs 1 and 2 |
| Model 3b, 2 | 2 | 2 | 50 | 469 | 200 | 5.7 | 90 | 180 | 0.124 | 0.081 | 49 high | 16 Calibration adjusted to bring into line with ppt2 |
| Model 3b, 2 | 2 | 2 | 50 | 528 | 228 | 4.5 | 82 | 186.96 | 0.117 | 0.076 | 49 high | 2 Good record |
| Model 3b, 2 | 2 | 2 | 50 | 385 | 164 | 25.1 | 90 | 147.6 | 0.132 | 0.086 | 49 high | 11 Clearly reached limit |
| Model 3b, 3 | 3 | 3 | 50 | 466 | 190 | 5.157 | 85 | 161.5 | 0.135 | 0.088 | 50 med | 1 Just reached limit |
| Model 3b, 3 | 3 | 3 | 50 | 469 | 197 | 4.887 | 90 | 177.3 | 0.135 | 0.088 | 50 high | 16 Calibration adjusted to bring into line with ppt2 |
| Model 3b, 3 | 3 | 3 | 50 | 528 | 220 | 6.5 | 66 | 145.2 | 0.127 | 0.083 | 50 high | 2 Good record |
| Model 3b, 3 | 3 | 3 | 50 | 385 | 164 | 19.7 | 90 | 147.6 | 0.144 | 0.093 | 50 high | 11 Clearly reached limit |
| Model 3c, 1 | 1 | 1 | 50 | 457 | 194 | 4.266 | 100 | 194 | 0.225 | 0.146 | 50 * | 1 Just reached limit |
| Model 3c, 1 | 1 | 1 | 50 | 468 | 196 | 4.05 | 100 | 196 | 0.228 | 0.148 | 50 * | 30 Excellent, exactly 100%, less than 1 cycle to 50% query amplitude |
| Model 3c, 1 | 1 | 1 | 50 | 524 | 222 | 4.16 | 95 | 210.9 | 0.216 | 0.141 | 50 * | 31 Excellent, again exactly 100% |
| Model 3c, 1 | 1 | 1 | 50 | 296 | 130 | 17.55 | 87 | 113.1 | 0.247 | 0.161 | 75 high | 10 Excellent |
| Model 3c, 1 | 1 | 1 | 50 | 320 | 129 | 14.85 | 90 | 116.1 | 0.268 | 0.174 | 75 high | 11 Limit rises slowly |
| Model 3c, 1 | 1 | 1 | 50 | 382 | 160 | 7.506 | 100 | 160 | 0.243 | 0.158 | 75 high | 16 Limit rises slowly |
| Model 3c, 1 | 1 | 1 | 50 | 115 | 53.5 | 5.4 | 84 | 44.94 | 0.3 | 0.195 | 75 high | 15 Rapid rise time, liquefaction could be affected by loose layer below |
| Model 3c, 1 | 1 | 1 | 50 | 123 | 54 | 6.8 | 96 | 51.84 | 0.315 | 0.205 | 75 high | 5 Clear limit, noisy record affects 50% |
| Model 3c, 1 | 1 | 1 | 50 | 252 | 100 | 9.5 | 96 | 96 | 0.296 | 0.192 | 75 high | 2 Clear limit, noisy record affects 50% |
| Model 3c, 2 | 2 | 2 | 50 | 457 | 194 | 6.534 | 98 | 190.12 | 0.218 | 0.142 | 50 high | 1 Limit rises slowly affects 50% |
| Model 3c, 2 | 2 | 2 | 50 | 468 | 196 | 5.67 | 96 | 188.16 | 0.221 | 0.143 | 50 high | 30 Rapid rise to 90% + |
| Model 3c, 2 | 2 | 2 | 50 | 524 | 222 | 12 | 92 | 204.24 | 0.209 | 0.136 | 50 med | 31 Very rapid rise to 90% + |
| Model 3c, 2 | 2 | 2 | 50 | 296 | 130 | 37.8 | 90 | 117 | 0.239 | 0.156 | 76 low | 10 First limit reached at 82%, then rose to 92% |
| Model 3c, 2 | 2 | 2 | 50 | 320 | 129 | 36.8 | 92 | 118.68 | 0.26 | 0.169 | 75 low | 11 Still climbing slowly at end of shaking |
| Model 3c, 2 | 2 | 2 | 50 | 382 | 160 | 21.6 | 100 | 160 | 0.235 | 0.153 | 75 high | 16 Still climbing slowly at end of shaking |
| Model 3c, 2 | 2 | 2 | 50 | 115 | 53.5 | 24.3 | 77 | 41.195 | 0.29 | 0.189 | 75 high | 15 Reached limit, probably influenced by loose layer below |
| Model 3c, 2 | 2 | 2 | 50 | 123 | 54 | 32.4 | 83 | 44.82 | 0.305 | 0.198 | 75 high | 5 Clear limit, noisy record |
| Model 3c, 2 | 2 | 2 | 50 | 252 | 100 | 31.1 | 95 | 95 | 0.286 | 0.186 | 75 high | 2 Clear limit, noisy record |
| Model 3c, 3 | 3 | 3 | 50 | 457 | 194 | 8.1 | 97 | 188.18 | 0.207 | 0.134 | 50 high | 1 Close to 100% at end of shaking |
| Model 3c, 3 | 3 | 3 | 50 | 468 | 196 | 7.641 | 98 | 192.08 | 0.209 | 0.136 | 50 high | 30 Rapid rise to 90% + |
| Model 3c, 3 | 3 | 3 | 50 | 524 | 222 | 15.3 | 95 | 210.9 | 0.199 | 0.129 | 50 med | 31 Very rapid rise to 90% + |
| Model 3c, 3 | 3 | 3 | 50 | 296 | 130 | 44.33 | 92 | 119.6 | 0.227 | 0.148 | 75 low | 10 Again, double stage rise, as eq2 |
| Model 3c, 3 | 3 | 3 | 50 | 320 | 129 | 45.9 | 93 | 119.97 | 0.246 | 0.16 | 75 low | 11 Still climbing slowly at end of shaking |
| Model 3c, 3 | 3 | 3 | 50 | 382 | 160 | 22.7 | 100 | 160 | 0.223 | 0.145 | 75 high | 16 Still climbing slowly at end of shaking |
| | | | | | | | | | | | | 15 Probably influenced by loose layer below |

| | | | | | | | | | | | | |
|-------------|---|-----|-----|------|------|----|--------|-------|-------|---------|----|--|
| Model 3c, 3 | 3 | 50 | 115 | 53.5 | 24.3 | 76 | 40.66 | 0.275 | 0.179 | 75 high | 5 | Clear limit, noisy record |
| Model 3c, 3 | 3 | 50 | 123 | 54 | 23 | 82 | 44.28 | 0.29 | 0.188 | 75 high | 2 | Clear limit, noisy record |
| Model 3c, 3 | 3 | | | | | | | | | | 1 | Still rising at end of shaking |
| Model 3d, 1 | 1 | 125 | 434 | 226 | 8.6 | 63 | 142.38 | 0.147 | 0.09 | 54 * | 48 | Excellent |
| Model 3d, 1 | 1 | 125 | 515 | 245 | 17.6 | 78 | 191.1 | 0.147 | 0.095 | 54 med | 37 | Slow buildup makes definition of limit difficult |
| Model 3d, 1 | 1 | 125 | 522 | 243 | 12.4 | 75 | 182.25 | 0.149 | 0.097 | 54 high | 35 | Slow buildup makes definition of limit difficult |
| Model 3d, 1 | 1 | 125 | 434 | 223 | 7.9 | 65 | 144.95 | 0.141 | 0.092 | 54 * | 40 | Excellent, cycles affect 50% |
| Model 3d, 1 | 1 | | | | | | | | | | 38 | Still climbing at end of shaking |
| Model 3d, 1 | 1 | | | | | | | | | | 44 | Still climbing at end of shaking |
| Model 3d, 2 | 2 | 125 | 523 | 283 | 14.8 | 70 | 198.1 | 0.163 | 0.106 | 54 high | 37 | Rapid rise to 60%, then slow climb |
| Model 3d, 2 | 2 | 125 | 522 | 273 | 11.8 | 73 | 199.29 | 0.169 | 0.11 | 54 high | 35 | Rapid rise to 60%, then slow climb |
| Model 3d, 2 | 2 | | | | | | | | | | 48 | Still climbing slowly at end of shaking |
| Model 3d, 2 | 2 | | | | | | | | | | 40 | Still climbing at end of shaking |
| Model 3d, 2 | 2 | | | | | | | | | | 38 | Still climbing at end of shaking |
| Model 3d, 2 | 2 | | | | | | | | | | 44 | Still climbing at end of shaking |
| Model 3d, 3 | 3 | 125 | 523 | 283 | 8 | 70 | 198.1 | 0.168 | 0.109 | 54 high | 37 | Good record |
| Model 3d, 3 | 3 | 125 | 522 | 273 | 8.5 | 75 | 204.75 | 0.174 | 0.113 | 54 high | 35 | Good record |
| Model 3d, 3 | 3 | | | | | | | | | | 48 | Still climbing slowly at end of shaking |
| Model 3d, 3 | 3 | | | | | | | | | | 40 | Still climbing at end of shaking |
| Model 3d, 3 | 3 | | | | | | | | | | 38 | Still climbing at end of shaking |
| Model 3d, 3 | 3 | | | | | | | | | | 44 | Still climbing at end of shaking |
| Model 3d, 4 | 4 | 125 | 508 | 268 | 28.6 | 72 | 192.96 | 0.182 | 0.118 | 54 high | 37 | Two stage rise |
| Model 3d, 4 | 4 | 125 | 522 | 273 | 27.2 | 70 | 191.1 | 0.184 | 0.12 | 54 high | 35 | Two stage rise |
| Model 3d, 4 | 4 | 125 | 435 | 257 | 28.1 | 62 | 159.34 | 0.171 | 0.111 | 54 high | 48 | Clear limit |
| Model 3d, 4 | 4 | 125 | 438 | 257 | 25.9 | 61 | 156.77 | 0.172 | 0.112 | 54 high | 40 | Clear limit |
| Model 3d, 4 | 4 | | | | | | | | | | 38 | Still climbing at end of shaking |
| Model 3d, 4 | 4 | | | | | | | | | | 44 | Still climbing at end of shaking |
| Model 4a, 1 | 1 | 50 | 477 | 347 | 24.8 | 80 | 277.6 | 0.078 | 0.051 | 49 high | 45 | Clearly reached upper limit |
| Model 4a, 1 | 1 | 50 | 483 | 348 | 26.7 | 75 | 261 | 0.078 | 0.051 | 49 high | 35 | Clearly reached upper limit |
| Model 4a, 1 | 1 | | | | | | | | | | 52 | Still climbing at end of shaking |
| Model 4a, 1 | 1 | | | | | | | | | | 43 | Still climbing at end of shaking |
| Model 4a, 2 | 2 | 50 | 469 | 339 | 40 | 27 | 91.53 | 0.098 | 0.064 | 49 med | 45 | Reached some sort of limit, much less than eq1 |
| Model 4a, 2 | 2 | 50 | 474 | 340 | 40 | 16 | 54.4 | 0.098 | 0.064 | 49 med | 35 | Reached some sort of limit, much less than eq1 |
| Model 4a, 2 | 2 | | | | | | | | | | 52 | Still climbing at end of shaking |
| Model 4a, 2 | 2 | | | | | | | | | | 43 | Still climbing at end of shaking |
| Model 4a, 3 | 3 | | | | | | | | | | 45 | Very little excess pore pressure generated |

| | | |
|-------------|---|--|
| Model 5b, 2 | 2 | 38 Rising steadily at end of shaking |
| Model 5b, 2 | 2 | 47 Rising steadily at end of shaking |
| Model 5b, 2 | 2 | 46 Rising steadily at end of shaking |
| Model 5b, 2 | 2 | 50 Rising steadily at end of shaking |
| Model 5b, 2 | 2 | 41 Rising steadily at end of shaking |
| Model 5b, 3 | 3 | 51 Small excess pore pressure, rising steadily at end of shaking |
| Model 5b, 3 | 3 | 38 Small excess pore pressure, rising steadily at end of shaking |
| Model 5b, 3 | 3 | 47 Small excess pore pressure, rising steadily at end of shaking |
| Model 5b, 3 | 3 | 46 Small excess pore pressure, rising steadily at end of shaking |
| Model 5b, 3 | 3 | 50 Almost no excess pore pressure, slight rise at end of shaking |
| Model 5b, 3 | 3 | 41 Almost no excess pore pressure, slight rise at end of shaking |
| Model 5b, 4 | 4 | 51 Very little excess pore pressure |
| Model 5b, 4 | 4 | 38 Very little excess pore pressure |
| Model 5b, 4 | 4 | 47 Almost no excess pore pressure |
| Model 5b, 4 | 4 | 46 Almost no excess pore pressure |
| Model 5b, 4 | 4 | 50 Very little excess pore pressure |
| Model 5b, 4 | 4 | 41 Very little excess pore pressure |
| Model 5c, 1 | 1 | 46 Almost no excess pore pressure, noisy signal |
| Model 5c, 1 | 1 | 47 Almost no excess pore pressure, noisy signal |
| Model 5c, 1 | 1 | 41 Still climbing at end of shaking |
| Model 5c, 1 | 1 | 50 Still climbing at end of shaking |
| Model 5c, 1 | 1 | 38 Starting to climb steeply at end of shaking |
| Model 5c, 1 | 1 | 51 Starting to climb steeply at end of shaking |
| Model 5c, 2 | 2 | 46 Climbing at end of earthquake |
| Model 5c, 2 | 2 | 47 Climbing at end of earthquake |
| Model 5c, 2 | 2 | 41 Climbing at end of earthquake |
| Model 5c, 2 | 2 | 50 Climbing at end of earthquake |
| Model 5c, 2 | 2 | 38 Climbing steeply at end of shaking |
| Model 5c, 2 | 2 | 51 Climbing steeply at end of shaking |
| Model 5c, 3 | 3 | 46 Climbing at end of earthquake |
| Model 5c, 3 | 3 | 47 Climbing at end of earthquake |
| Model 5c, 3 | 3 | 41 Climbing at end of shaking, but possible flat top just at end |
| Model 5c, 3 | 3 | 50 Climbing at end of earthquake |

| Model | 5c, 3 | 3 | 50 | 1291 | 1009 | 28 | 17 | 171.53 | 0.042 | 0.028 | 52 low | 38 Climbing steadily at end of shaking |
|-------------|-------|---|----|------|------|------|----|--------|-------|-------|---------|---|
| Model 5c, 3 | 3 | 3 | 50 | 1291 | 1009 | 28 | 17 | 171.53 | 0.042 | 0.028 | 52 low | 51 Climbing at end of shaking, but possible flat top just at end |
| Model 5d, 1 | 1 | 1 | 50 | 1223 | 978 | 47.3 | 33 | 322.74 | 0.092 | 0.06 | 39 high | 31 Filtered acceleration record : (note 6 ppts in upper layer showed) |
| Model 5d, 1 | 1 | 1 | 50 | 1217 | 985 | 37 | 35 | 344.75 | 0.091 | 0.059 | 39 high | 43 Filtered acceleration record : no significant response during shaking) |
| Model 5d, 1 | 1 | 1 | 50 | 1280 | 1037 | 34.4 | 52 | 539.24 | 0.088 | 0.047 | 39 high | 39 Filtered acceleration record |
| Model 5d, 1 | 1 | 1 | | | | | | | | | | 13 Climbing at end of shaking |

APPENDIX B

Stress path analysis

APPENDIX B: CALCULATION OF THE STRESS PATH

The stress path followed by an element in the sand bed was calculated in s', t space using the time history of shear stress computed from the acceleration record. Two models were selected for first analysis, Model 3c, earthquake 1 and Model 5d, earthquake 1. In Model 3c, ppt 30 showed clear evidence of liquefaction after 4.3 cycles, reaching 100% of the initial vertical effective stress with a cyclic stress ratio $t/\sigma_v' = 0.155$. As described previously, Steedman (1999a), the cyclic stress ratio is calculated as 0.65 times the peak stress ratio of 0.239, following conventional practice. In the case of Model 3c, the peak stress ratio was based on the smoothed acceleration input from acc 12609 (at the bottom of the sand bed). In Model 5d, the pore pressure in the loose layer reached a peak level of around 52% of the initial effective vertical stress, partway through the shaking, and then was capped. This observation prompted a closer examination of the stress paths being followed at these locations in the models.

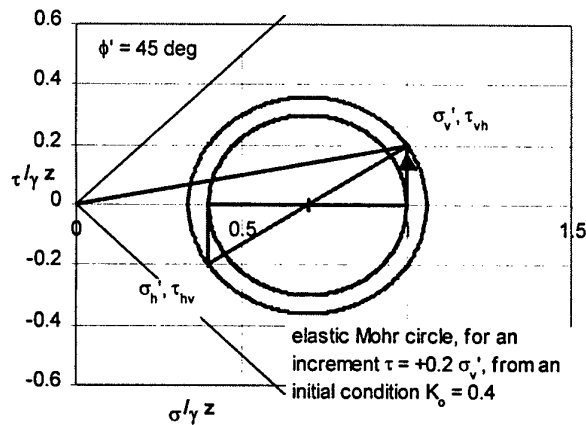


Figure B.1

To calculate the stress path, the stress ratio of shear stress to initial effective vertical stress was used first to compute the applied shear stress on a horizontal plane as a function of time, using the time history. The stress on a vertical plane is given by

$$\sigma_h' = K_o \sigma_v'.$$

Shear stress applied to horizontal (and vertical) planes causes the Mohr circle to dilate, without change in the mean effective stress, s' , as shown in Figure B.1.

In this (elastic) condition, prior to yield, it may be shown that

$$s' = 0.5 \sigma_v' (1 + K_o), \text{ and}$$

$$t = 0.5 \{ \sigma_v' (1 - K_o)^2 + 4 \tau^2 \}^{0.5}$$

Once the stress state reaches a condition of yield, denoted by a maximum mobilised angle of shearing resistance, ϕ'_{max} , as shown in Figure B.2, then further increase in the applied shear stress on a horizontal plane forces the mean effective confining

stress to increase, as the circle is constrained by the ϕ'_{\max} line. In this 'yielding' condition it may be shown that

$$s' = \sigma'_v \{ \sec^2 \phi'_{\max} \pm \sec \phi'_{\max} \sqrt{(\tan^2 \phi'_{\max} - \tan^2 \beta)} \}, \text{ and}$$

$$t = s' \sin \phi'_{\max}$$

where $\tan \beta = \tau/\sigma'_v = (\tau/\sigma'_{v0}) \sigma'_{v0}/\sigma'_v$. A more extensive discussion of this approach as adopted for the calculation of stress paths behind a retaining wall was presented by Steedman (1999b).

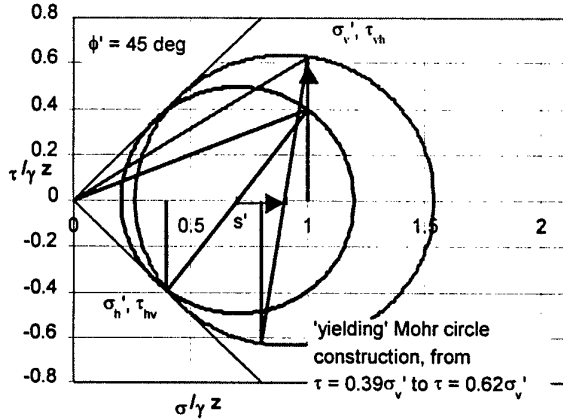


Figure B.2 Example of the dilation of a 'yielding' stress state

At any stage, the mobilised angle of shearing resistance may be simply calculated as

$$\phi'_{\text{mob}} = \text{asin}(s'/t)$$

As excess pore pressure develops, the vertical effective stress is reduced, and s' is also reduced. Assuming that K_0 is constant, then the radius of the Mohr's circle, given by t , must also reduce. Depending on the amplitude of the applied shear stress and the rate of generation of excess pore pressure, the stress path may be driven onto the yield surface or not.

The parameter K_0 is seen to be fundamental to the prediction of the stress path, both in its initial value and in the assumption that it is constant at any stage prior to liquefaction.

Following this approach, the stress paths were computed for Model 3c and 5d. Figure B.3 shows the pore pressure, acceleration and stress ratio for Model 3c associated with ppt 30, at mid depth in the loose layer, under an initial vertical effective stress of 194 KPa (1.8 tsf).

Two values of K_0 were used, $K_0 = 1$ and $K_0 = 1 - \sin \phi'_{\max}$. Figure B.4 shows the stress path in s' - t space for ppt 30, assuming $K_0 = 1$. Figures B.5 and B.6 show the progression over time of s' and t respectively. Figure B.7 shows the mobilised angle of shearing resistance.

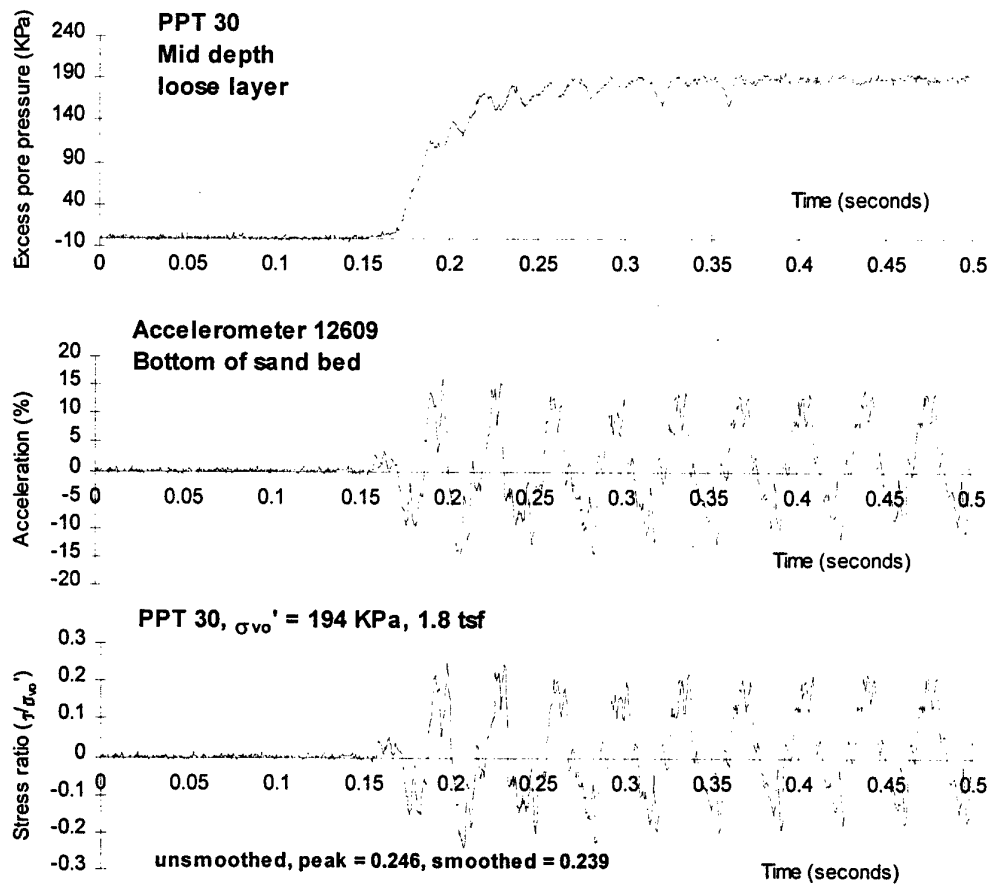


Figure B.3 Time histories of pore pressure, acceleration and shear stress ratio, Model 3c

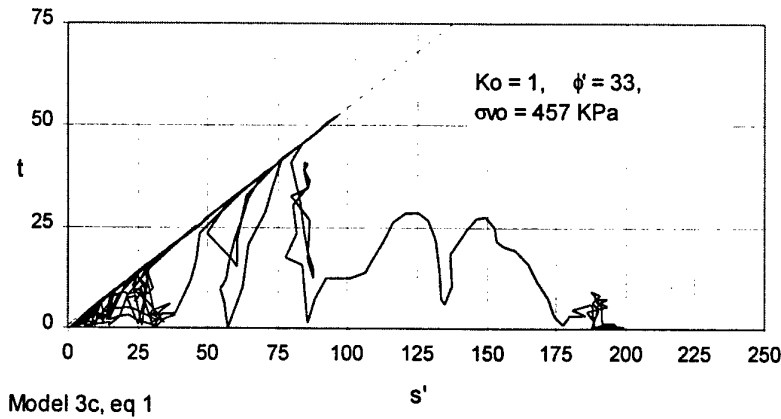


Figure B.4 Stress path at mid-depth in loose layer, Model 3c, earthquake 1 ($K_0 = 1$)

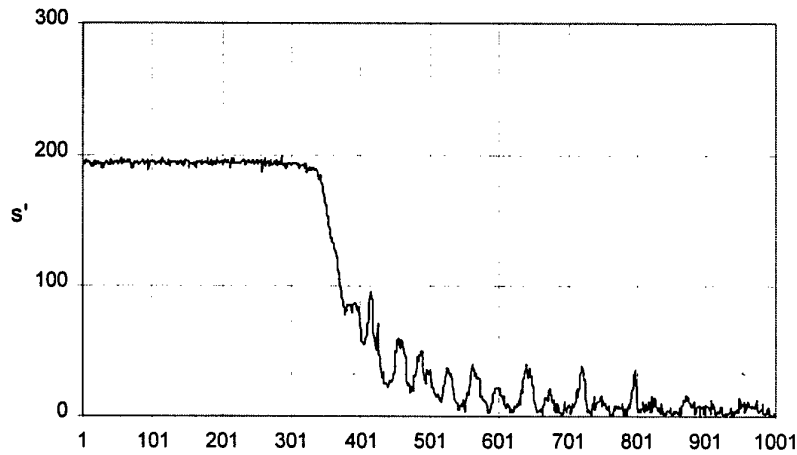


Figure B.5 Mean effective confining stress at mid-depth in loose layer, Model 3c ($K_o=1$)

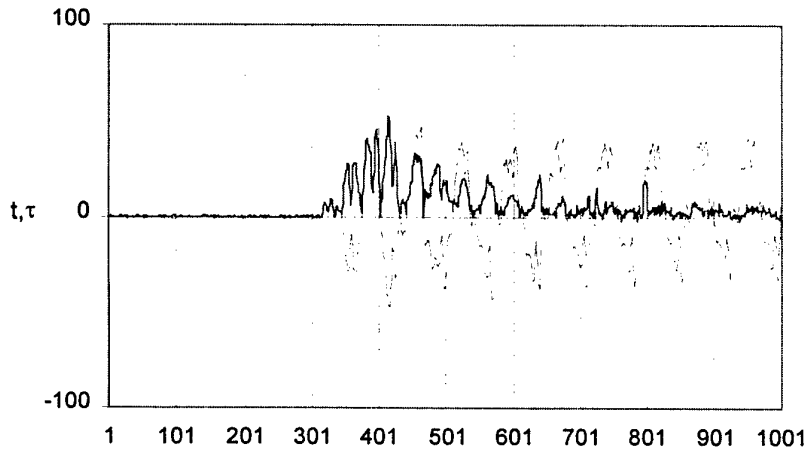


Figure B.6 Shear stress t and applied shear stress τ as function of time, Model 3c ($K_o=1$)

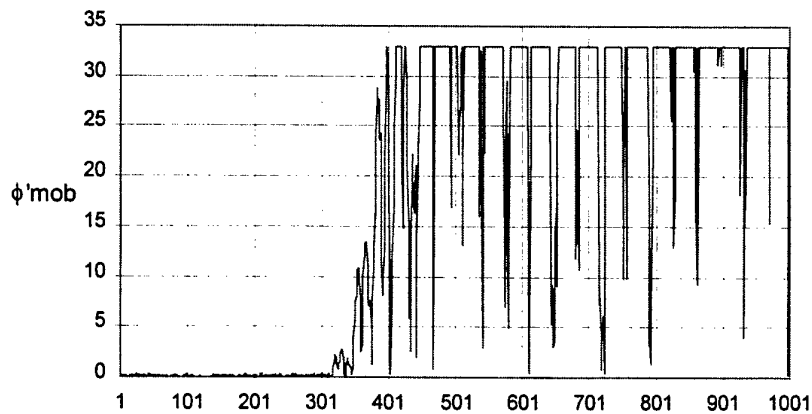


Figure B.7 Mobilised angle of shearing resistance, Model 3c ($K_o=1$)

For $K_o = 1 - \sin \phi'_{max}$, then $K_o = 0.455$. This has a dramatic effect on the predicted stress path in s' , t space, Figure B.8.

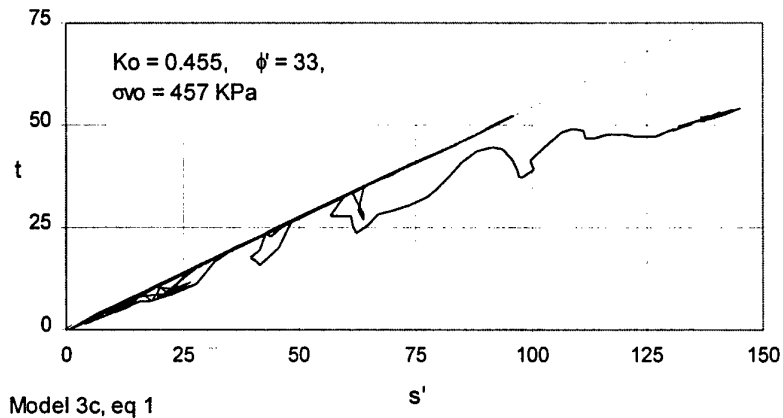


Figure B.8 Stress path for $K_o = 0.455$, Model 3c, earthquake 1

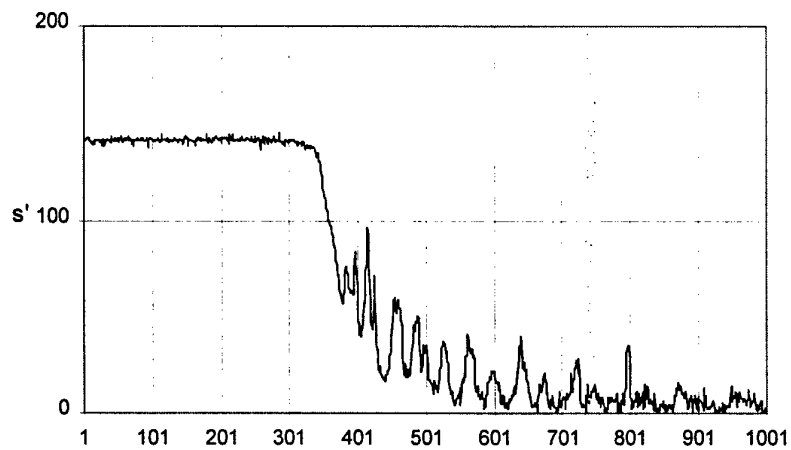


Figure B.9 Mean effective confining stress, s' , for $K_o = 0.455$, Model 3c

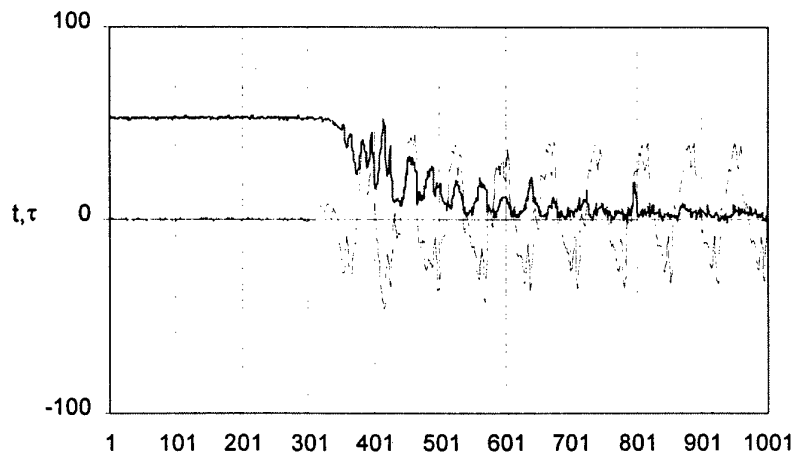


Figure B.10 Shear stress for $K_o = 0.455$, Model 3c

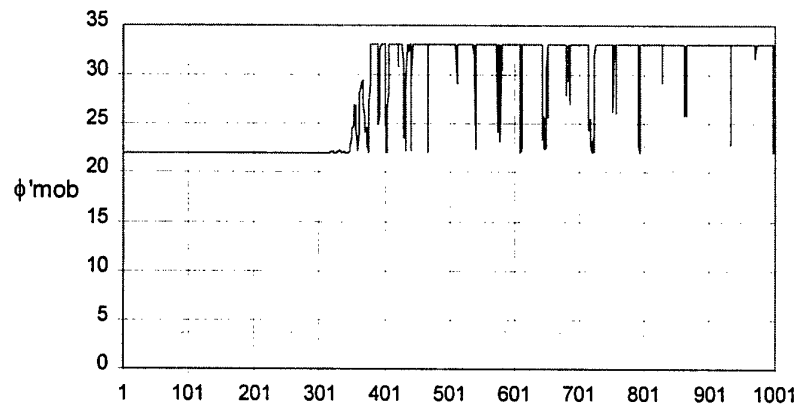


Figure B.11 Mobilised angle of shearing resistance, $K_o = 0.455$, Model 3c

Model 5d showed a rise in excess pore pressure in the loose layer, which reached a limiting value partway through the shaking event. Such behaviour has been observed in laboratory tests, Ishihara (1996).

Figure B.12 shows the pore pressure at mid-depth in the loose layer, the acceleration and shear stress time histories for Model 5d, earthquake 1. The initial vertical effective stress was 1037 KPa (9.7 tsf).

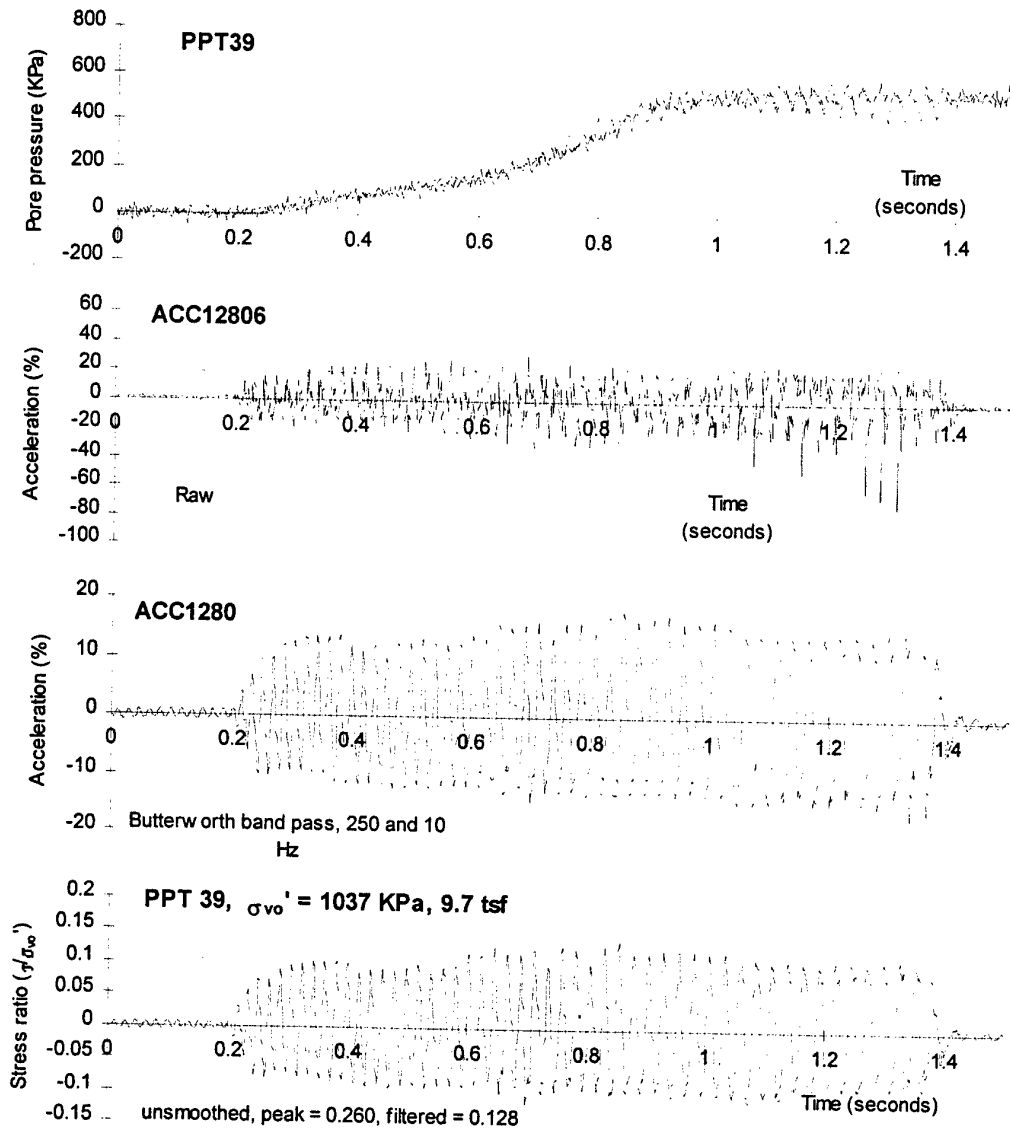
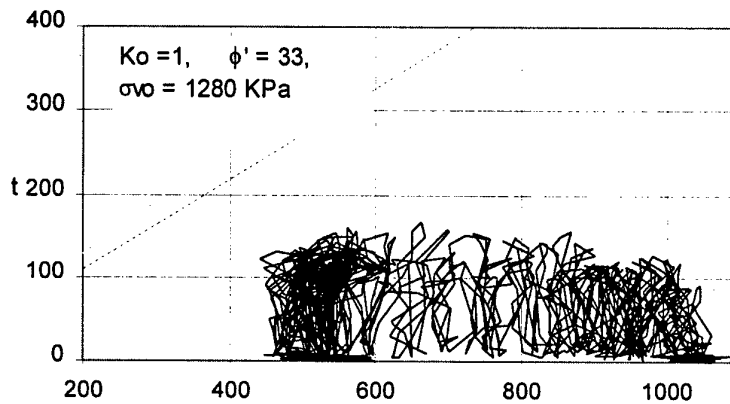


Figure B.12 Time histories of pore pressure, acceleration and applied shear stress for Model 5d, earthquake 1, at mid-depth in the loose layer

Figure B.12 also shows a comparison between the raw and filtered (Butterworth band pass filter, low 250 Hz, high 10 Hz) acceleration records. The filtered time history was used for computing the applied shear stress because it was considered to be a more accurate representation of the true strain history in the soil specimen, without the high frequency noise distortion, particularly towards the end of the earthquake.

For Model 5d, the analysis shows that with the stress path does not reach a yield condition, staying well below the yield surface for $K_0 = 1$, Figure B.13.



Model 5d, eq 1

Figure B.13 Stress path for Model 5d, earthquake 1, $K_0 = 1$

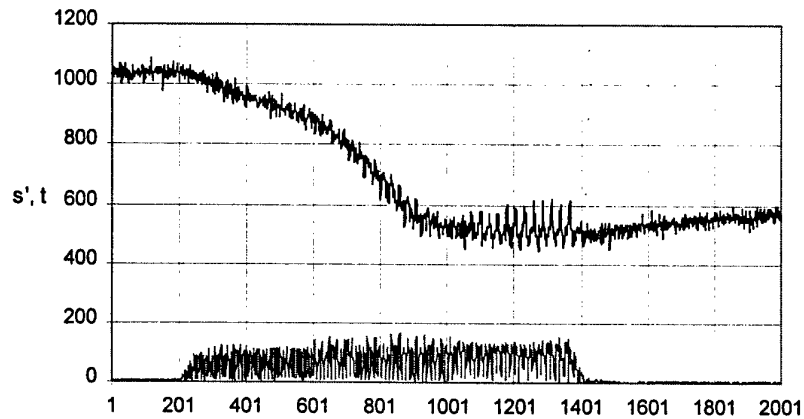


Figure B.14 mean effective confining stress, Model 5d, earthquake 1, $K_0 = 1$

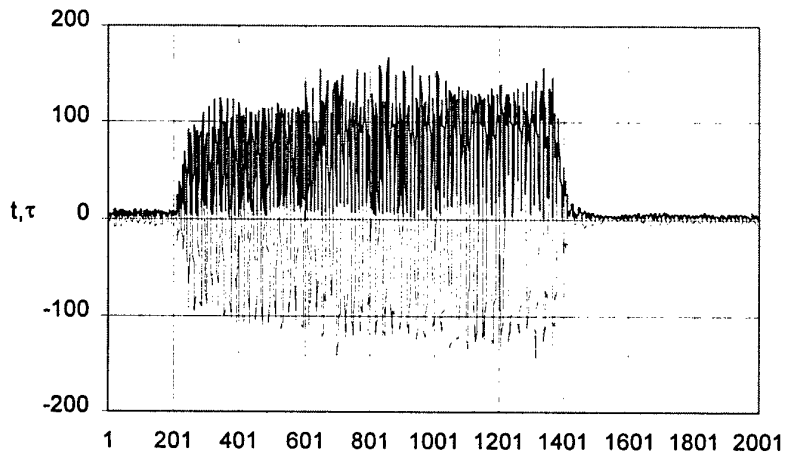


Figure B.15 Shear stress t and applied shear stress τ for Model 5d, earthquake 1, $K_o = 1$

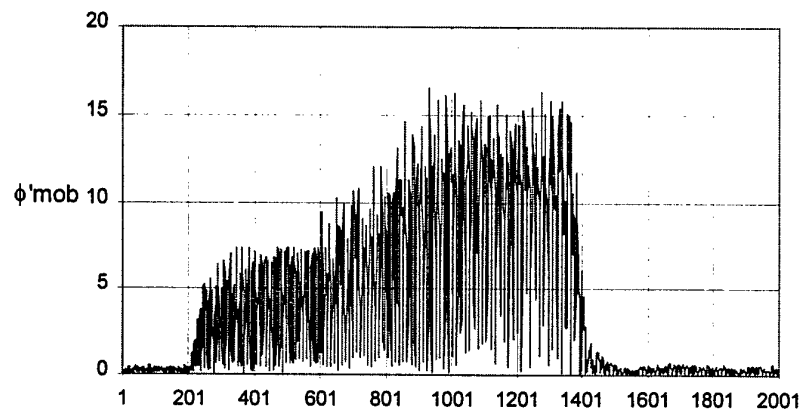
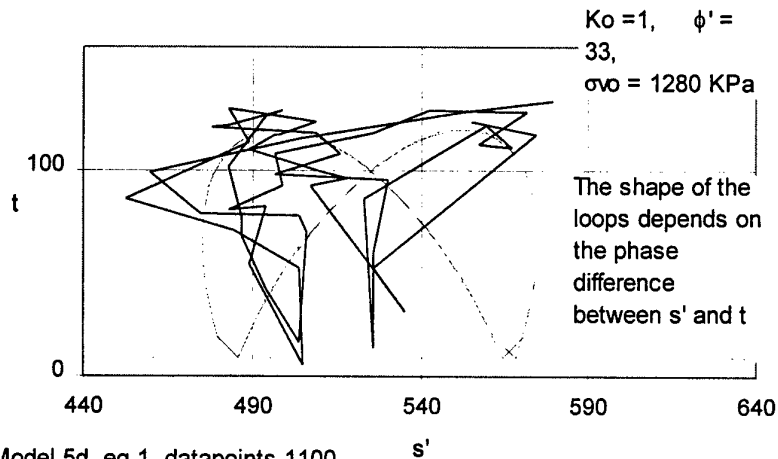


Figure B.16 Mobilised angle of shearing resistance, Model 5d, earthquake 1, $K_o = 1$

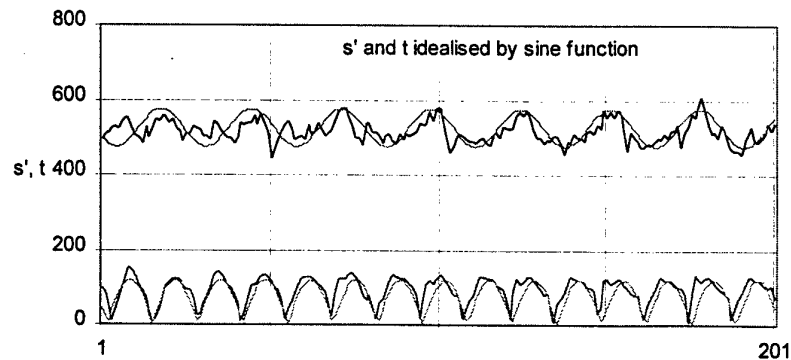
The detail of the stress path was examined by windowing the data to examine a short period during the shaking when the mean effective stress was 'capped' at around 52%. The stress path for around two cycles of s' is shown in Figure B.17.



Model 5d, eq 1, datapoints 1100-1150

Figure B.17 Stress path for two cycles of s' , Model 5d, earthquake 1, $K_o = 1$

Also shown in Figure B.17 is a theoretical shape for the path, assuming that s' and t may be represented by sine functions. Figure B.18 and B.19 show the paths in mean effective stress and shear stress, together with the arbitrary sine functions used to model the fluctuations with time. In all of these figures, the x axis is the number of data points.



Model 5d, eq 1, datapoints 1000-1200

Figure B.18 Enlargement showing detail of s' and t during 'capped' portion of shaking

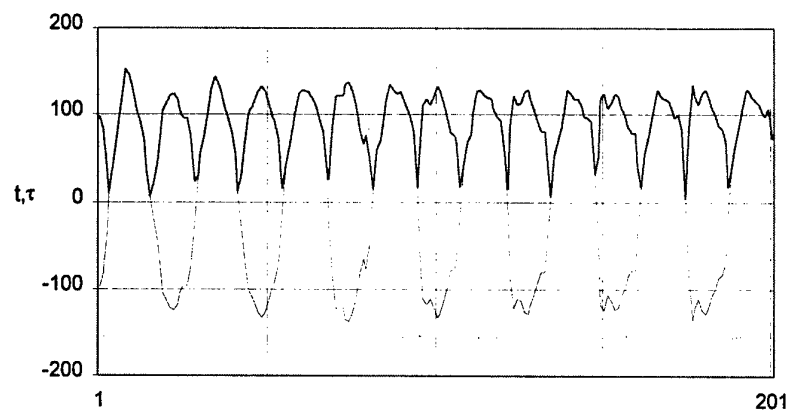


Figure B.19 Comparison between applied shear stress and t

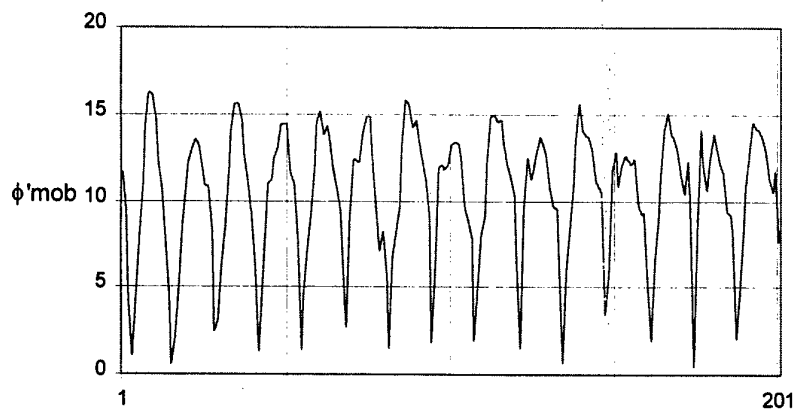
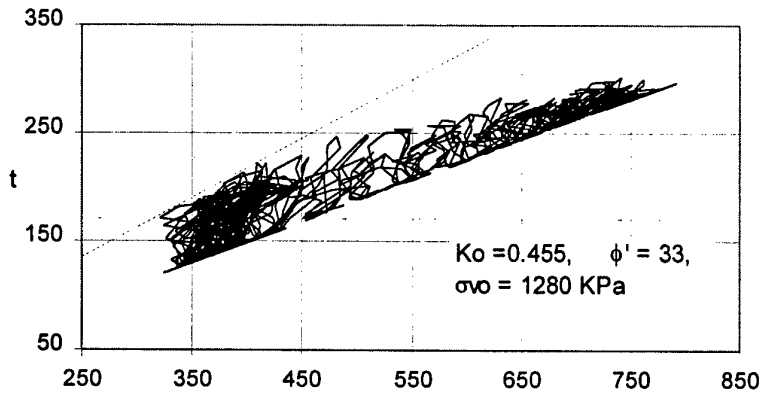


Figure B.20 Mobilised angle of shearing resistance

Figure B.20 shows the mobilised angle of shearing resistance for Model 5d, earthquake 1, for the condition $K_o = 1$.

Similarly to Model 3c, the stress path at mid-depth in the loose layer is changed dramatically in the case of a smaller K_o . Using a new value of $K_o = 0.455$, the stress path was recalculated for Model 5d, earthquake 1, Figure B.21.



Model 5d, eq 1

Figure B.21 Stress path for Model 5d, earthquake 1, for $K_o = 0.455$

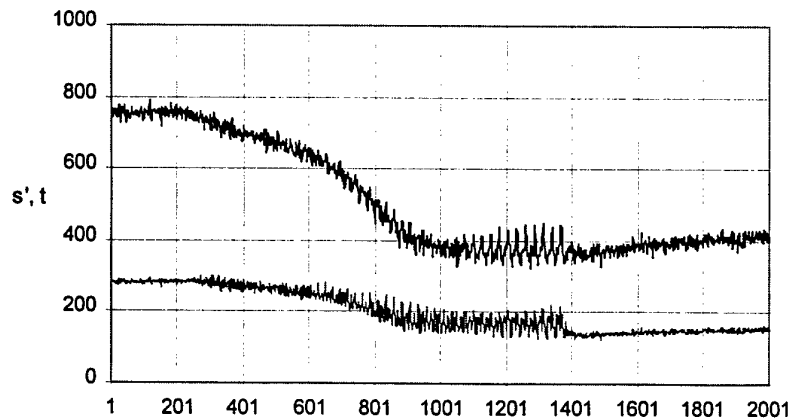


Figure B.22 s' and t , during Model 5d, earthquake 1, for $K_o = 0.455$

Figure B.22 shows the shear stress as a function of time.

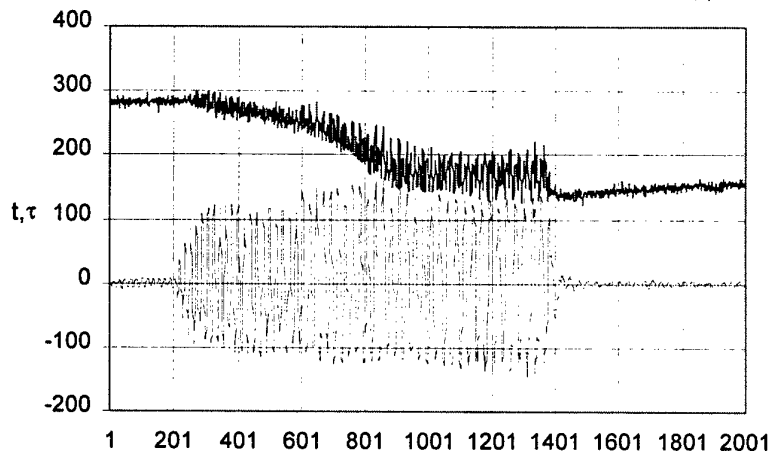


Figure B.23 Comparison between applied shear stress and t for Model 5d, earthquake 1, $K_o = 0.455$

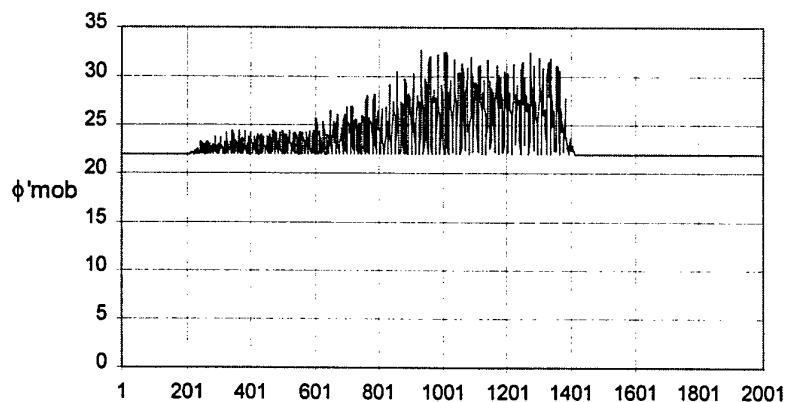


Figure B.24 Mobilised angle of shearing resistance, Model 5d, earthquake 1, $K_o = 0.455$

REFERENCES

- Bolton M D (1986) The strength and dilatancy of sands, *Geotechnique* 36, No. 1, pp 65-78.
- Hynes M E (1998) Influence of confining stress on liquefaction resistance, *Proc Int Workshop on the Physics and Mechanics of Soil Liquefaction*, Baltimore, MD, 10-11 Sept 1998, A A Balkema.
- Ishihara, K (1996) Soil behaviour in earthquake geotechnics, Clarendon Press, Oxford.
- Newland D E and Butler G D (1998) Application of time-frequency analysis to strong motion data with damage, *Proc 69th Shock and Vibration Symp*, Session HB1, SAVIAC, Minneapolis.

- Newland D E and Butler G D (1999) Time-varying cross-spectra for soil motion with damage, 17th ASME Biennial Conference on Mechanical Vibration and Noise, Proc 1999 ASME Design Engineering Tech Conf, Sept 12-15, Las Vegas.
- Olsen R S (1994) Normalisation and prediction of geotechnical properties using the Cone Penetrometer Test (CPT), PhD Dissertation, University of California, Berkeley.
- PHRI (1997) Handbook on liquefaction remediation of reclaimed land, Balkema.
- Seed R B and Harder L F (1990) SPT-Based analysis of cyclic pore pressure generation and undrained residual strength; Proc. H Bolton Seed Memorial Symposium, Vol. 2, pp 351 - 376, BiTech Publishers Ltd, Vancouver.
- Steedman R S (1984) Modelling the behaviour of retaining walls in earthquakes, PhD Thesis, Cambridge University.
- Steedman R S (1997) Development of a Centrifuge Model Test Program for the study of liquefaction, Final Technical Report, European Research Office of the US Army, London, Contract N68171-97-C-9012.
- Steedman R S (1999a) Earthquake Engineering Support, Phase 2, Final Technical Report, USAE.
- Steedman R S (1999b) Seismic soil-structure interaction of rigid and flexible retaining walls, Proc 2nd Int Conf Geotechnical Earthquake Engineering, Lisbon, June.